OPEN ACCESS
IOP Publishing
Superconductor Science and Technology
Supercond. Sci. Technol. **38** (2025) 015013 (22pp)
https://doi.org/10.1088/1361-6668/ad9ad8

Physics-driven lumped-element modelling for impedance simulations of superconducting accelerator magnets

M Janitschke[1,2,*], M Bednarek[1], E Ravaioli[1], A P Verweij[1], G Willering[1] and U van Rienen[2]

[1] CERN, Meyrin, Switzerland
[2] University of Rostock, Rostock, Germany

E-mail: marvin.janitschke@cern.ch

Received 16 August 2024, revised 25 November 2024
Accepted for publication 5 December 2024
Published 13 December 2024

Abstract

Superconducting magnets in particle accelerators are subject to various forces, radiation, high voltages, or thermal gradients. These can cause failures such as inter-turn shorts, which can be very challenging to detect after the magnets are installed in the accelerator. Measurements in the time- and frequency domain can pinpoint outlier magnets or precursors of such failures. Interpretable, physics-driven simulations can facilitate this by studying if manufacturing tolerances cause the observed behaviour or if it can be correctly classified as an outlier. An equivalent circuit model is proposed to simulate superconducting accelerator magnets' impedances. The physics-driven model includes various coupled, non-linear effects in the superconductors, such as superconducting filament magnetisation, inter-filament and inter-strand coupling currents, eddy currents in the strands' copper and various magnet components, and stray capacitances. The model is validated against a wide range of available time- and frequency-domain measurements performed at the Large Hadron Collider at CERN. A very good agreement is achieved across the different measurements and domains. The network model is computationally very inexpensive while still preserving good accuracy and interpretability. The model can hence be used to reproduce impedances of superconducting magnets accurately for performance evaluations and to investigate the impact of failures.

Keywords: accelerator magnet, superconducting coil, fault diagnostics, frequency-domain, impedance measurements, AC-loss

1. Introduction

Superconducting magnets play a crucial role in particle accelerators, such as the Large Hadron Collider (LHC). Understanding their electrodynamic behaviour is essential for optimising their performance and ensuring reliability. The complex impedance as a function of frequency can give valuable insights into this behaviour. However, the impedances of superconducting magnets are generally difficult to interpret. The characterisation of the impedances of superconducting magnets and the establishment of an impedance baseline for their operational parameters serve to enhance the current understanding of superconducting magnet performance. Furthermore, they offer guidance on critical design considerations, which can be employed to minimise energy losses and optimise operational efficiency for future prototypes.

* Author to whom any correspondence should be addressed.

During their operation, the magnets are often subject to large forces, radiation, high voltages, and thermal gradients. With the expanding lifetime of such superconducting systems, the number of failures or breakdowns steadily increases and can cause some costly downtime. Faults, such as inter-turn short circuits, are very challenging to detect after the superconducting magnet is installed in the machine. Identifying those failures at an early stage or detecting precursors of breakdowns can help to significantly improve the reliability, availability, and performance of superconducting particle accelerators.

Measurements of the complex impedance, as a function of the frequency, are used to evaluate the electromagnetic behaviour across a wide range of regimes and conditions. Similar approaches to detect faults and to ensure electrical integrity were already used in the past, for example, for short-circuit detection in non-planar coils in fusion stellarators [1, 2], in CICC model coils [3], and for monitoring and controlling the resin impregnation process in Nb_3Sn coils [4]. Other approaches try to detect failures by applying machine learning algorithms to large data sets of time-domain measurements and to spot anomalies [5].

However, to apply these types of measurements or analyses for fault or non-conformity detection, it is necessary to obtain a detailed understanding of the observed measurements and ensure interpretability. A detailed and validated model of a superconducting magnet that captures its electromagnetic behaviour under various conditions and consistently across time and frequency domains can help in this endeavour. Moreover, utilising these models to simulate and investigate failure scenarios can shed more light on how failures manifest themselves in measurements in the time- and frequency domains, provide references for a variety of scenarios, and help in identifying promising measurement techniques that may be able to detect failures at an early stage.

Computationally inexpensive network models of superconducting magnets in the frequency domain have already been derived in the past. However, these models are not able to account for all important electromagnetic effects or incorporate their non-linear nature [6–13] or can not easily incorporate and simulate faults or non-conformities [14]. Other approaches lack physical interpretability as electromagnetic effects can not be directly mapped to specific components of the network model [15, 16]. Transient or time-domain simulations of superconducting magnets utilising various approaches exist widely. However, these approaches generally focus on single magnets and can not feasibly account for a chain of magnets. Other approaches, utilising network models for a chain of superconducting magnets, can provide valuable insights but can not incorporate non-linear, frequency-dependent behaviour and lack physical interpretability [10, 12].

This contribution describes the extended derivation and full validation of a recently developed equivalent lumped-element circuit model that can accurately reproduce the electrodynamic behaviour of a superconducting accelerator magnet in the time and frequency domain [17]. The paper is structured as follows: first, the general modelling approach of this two-dimensional network model will be described in section 2. The model accounts for various non-linear, dynamic effects such as inter-strand-coupling currents (ISCCs) (section 2.1), eddy currents in the copper of the conductors (section 2.2), inter-filament-coupling currents (IFCCs) (section 2.3) and persistent currents (PCs) and magnetisation (section 2.4) [18, 19]. Moreover, the model also incorporates eddy currents in the metallic components of the magnet, such as the beam screen (BS), cold bore (CB), copper wedges (W), and coil-protection sheets (CPSs) (sections 2.5 and 2.6). The equivalent lumped-element parameters for the network model are either derived utilising analytical equations or are pre-simulated by dedicated finite-element models (FEMs). As all of these dynamic effects are tightly connected, it is important to couple them in the model together. The derivation of the mutual coupling between all the effects will be described in section 2.7.

The model is validated against a wide range of available measurements of the superconducting LHC main dipole in section 3. The cross-section of the main dipole, including the considered metallic components, is shown in figure 1 and will be described in more detail in section 3.1. In section 3.2, the model is validated in the frequency domain against frequency transfer function measurements (TFMs) of a standalone dipole from CERN's magnet test facility at different temperatures, as well as against TFM performed on various magnets in the chain of magnets in the LHC tunnel. The effect of the BS eddy currents in the model is validated with dedicated special measurements. In section 3.3, the model validation in the time domain is presented. The simulation results are compared to signals acquired during fast power aborts (FPAs) in the LHC main dipole circuits. It is shown that the network model is very computationally inexpensive and hence, can be included in complex circuits comprising thousands of other components.

Section 4 summarises the findings of this work as guidance on design considerations for future high-field accelerator magnets. Finally, section 5 gives the conclusion and outlook.

2. Modelling approach

The lumped-element network model, aiming at reproducing the electromagnetic behaviour of a superconducting magnet in the time- and frequency-domain, includes the magnet's main inductance L_{mag} [H], which can be split up into smaller elements such as for example turn inductances. All these inductances are in series, each carrying a current I_{mag} [A], generating an applied magnetic flux density $\mathbf{B}_a$ [T] in the magnet. The series inductances are mutually coupled with M_{mag} [H]. Moreover, also resistances R_{mag} [Ω] are in series with these inductances, which are either the resistances of the magnet cables in the normal state or are zero in case the magnet is in the superconducting state. Finally, also stray capacitances to ground C_{GND} [F] are included.

Due to a changing current $\dot{I}_{\mathrm{mag}}$ [$\mathrm{A\,s^{-1}}$] flowing through the magnet coil, a field change $\dot{\mathbf{B}}_\mathbf{a}$ [$\mathrm{T\,s^{-1}}$] is introduced in the magnet components and conductors. According to

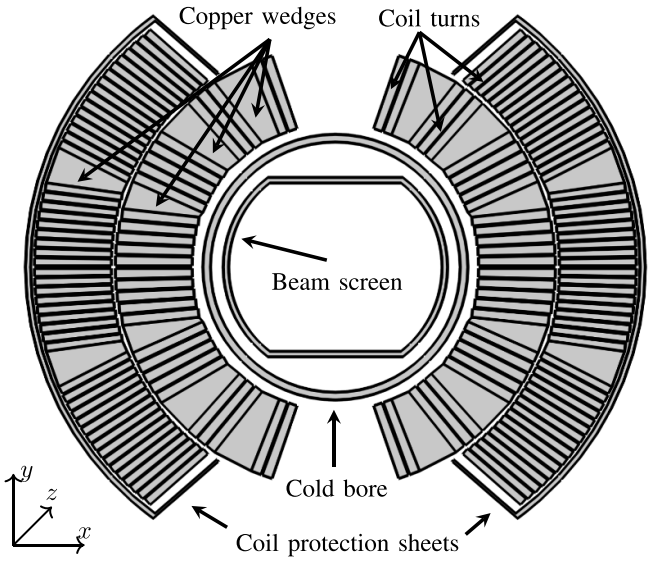

Figure 1. Cross-section of one aperture of the LHC main dipole magnet showing the coil turns, copper wedges, cold-bore, coil-protection sheets and beam-screen. The coil geometry is generated with [20].

Lenz's Law, the magnetic field change induces a specific current density $\mathbf{J_{ec}}$ [A m^2], totalling to an equivalent induced current I_{ec} [A]. The induced current density generates a field change $\dot{B}_{\mathbf{ec}}$ [T s^{-1}], opposing the applied field change. Within the volume where the current density is generated, the general relation between the total magnetic field change $\dot{B}_{\mathbf{tot}} = \dot{B}_{\boldsymbol{a}} + \dot{B}_{\mathbf{ec}}$ and the induced field change is defined by the time constant τ_{ec} [s] given in:

$$\mathbf{B_{ec}} = -\tau_{\mathrm{ec}}\dot{B}_{\mathbf{tot}} \qquad [\mathrm{T}]. \tag{1}$$

The induced eddy currents follow a given path, closing in a loop and can hence be represented by an equivalent inductance L_{ec} [H]. The induced currents generally flow or close through a resistive material, which can be represented by an equivalent resistance R_{ec} [Ω], generating a loss P_{ec} [W].

Based on these assumptions, each of the dynamic, non-linear effects can be represented by a coupling loop, consisting of the inductance L_{ec} and resistance R_{ec}, coupled to the respective inductance of the magnet with a mutual inductance M_{ec} [H]. A simplified example representing a magnet with two inductances, each coupled to two equivalent coupling loops, is shown in figure 2.

Consider a single coupled loop a, coupled to one magnet inductance $L_{\mathrm{mag},1}$. The respective voltage across one magnet inductance, coupled to n equivalent loops and p coil inductances, is:

$$V_{\mathrm{mag},1} = \dot{I}_{\mathrm{mag},1}L_{\mathrm{mag},1} + \sum_{x=1}^{n}\dot{I}_{\mathrm{ec},x}M_{\mathrm{ec},1,x} + \sum_{k=1}^{p}\dot{I}_{\mathrm{mag},k}M_{\mathrm{mag},1,k} \ [V], \tag{2}$$

In the following, we will perform the derivation in the 'open-circuit' configuration, assuming the current only flows through

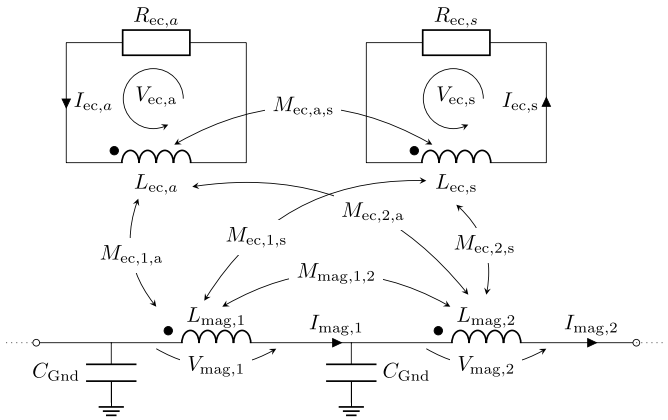

Figure 2. Equivalent lumped-element network model, showing the modelling approach with two equivalent loops coupled to the inductances of a magnet.

the inductance $L_{\mathrm{mag},1}$ (e.g. $I_{\mathrm{mag},k} = 0 \,\forall\, k \in [1,p]$). The voltage within the coupling loop can be calculated as follows:

$$V_{\mathrm{ec},a} = R_{\mathrm{ec},a}I_{\mathrm{ec},a} + \dot{I}_{\mathrm{ec},a}L_{\mathrm{ec},a} + M_{\mathrm{ec},1,a}\dot{I}_{\mathrm{mag},1} = 0 \qquad [\mathrm{V}], \tag{3}$$

giving the definition for the mutual coupling between the inductance of the equivalent loop and the magnet inductance. The equivalent lumped-element parameter for a general loop can then be calculated as:

$$R_{\mathrm{ec}} = \frac{P_{\mathrm{ec}}}{I_{\mathrm{ec}}^2} \qquad [\Omega], \tag{4}$$

$$L_{\mathrm{ec}} = \tau_{\mathrm{ec}}R_{\mathrm{ec}} \qquad [\mathrm{H}], \tag{5}$$

$$M_{\mathrm{ec}} = \begin{cases} \frac{\dot{I}_{\mathrm{ec}}L_{\mathrm{ec}} + R_{\mathrm{ec}}I_{\mathrm{ec}}}{\dot{I}_{\mathrm{mag}}} & \forall t \text{ s.t.} \dot{I}_{\mathrm{mag}} \neq 0 \\ 0 & \text{otherwise} \end{cases} \qquad [\mathrm{H}], \tag{6}$$

where I_{ec} is the equivalent induced current in the loop. One way to obtain such an equivalent current is to integrate the absolute value of the induced current density over the considered cross-section:

$$I_{\mathrm{ec}} = \frac{1}{2}\int_A |J_{\mathrm{ec}}| \,\mathrm{d}A \qquad [\mathrm{A}], \tag{7}$$

where half of the absolute value is needed, as otherwise, by the law of conservation of current, the integral would result in zero. P_{ec} is the total power loss generated by this equivalent induced current. The derivations in equations (4)–(6) assume I_{ec} and P_{ec} to be calculated without consideration of the other effects. Coupling between the different equivalent loops can also be included and will be described in section 2.7. Moreover, the mutual coupling of the loop with the magnet inductance is not defined for a constant magnet current, as no currents are induced.

One way of assessing the impact of a coupling effect is to look at the differential inductance of the magnet $L_{\mathrm{mag,D}}$ [H]. Assuming the flux linkage $\lambda(I_{\mathrm{mag}})$ [Wb] as a function of the current, the differential inductance is defined as the ratio of flux change over a given change of current $L_{\mathrm{mag,D}} = \frac{\mathrm{d}\lambda}{\mathrm{d}I}$. An

alternative definition can be found as the ratio of voltage across the magnet inductance and the current change:

$$L_{\mathrm{mag},1,\mathrm{D}} = \frac{V_{\mathrm{mag},1}}{\dot{I}_{\mathrm{mag},1}}. \tag{8}$$

By rearranging equation (3) for the induced current change $\dot{I}_{\mathrm{ec}}$:

$$\dot{I}_{\mathrm{ec},a} = -\frac{I_{\mathrm{ec},a}R_{\mathrm{ec},a} + M_{\mathrm{ec},1,a}\dot{I}_{\mathrm{mag},1}}{L_{\mathrm{ec},a}} \quad [\mathrm{A}]. \tag{9}$$

and dividing the voltage across the inductance in equation (2) by the current change, one obtains the differential inductance as:

$$L_{\mathrm{mag},1,\mathrm{D}} = \frac{V_{\mathrm{mag},1}}{\dot{I}_{\mathrm{mag},1}} \tag{10}$$

$$= L_{\mathrm{mag},1} - \frac{(M_{\mathrm{ec},1,a})^2}{L_{\mathrm{ec},a}} - \frac{R_{\mathrm{ec},a}I_{\mathrm{ec},a}M_{\mathrm{ec},1,a}}{L_{\mathrm{ec},a}\dot{I}_{\mathrm{mag},1}} \tag{11}$$

$$= L_{\mathrm{mag},1} - k^2 L_{\mathrm{mag},1} - \frac{M_{\mathrm{ec},1,a}}{\tau_{\mathrm{ec},a}}\frac{I_{\mathrm{ec},a}}{\dot{I}_{\mathrm{mag},1}} \quad [\mathrm{H}], \tag{12}$$

where we introduced the coupling coefficient $k = \frac{M_{\mathrm{ec}}}{\sqrt{L_{\mathrm{ec}}L_{\mathrm{mag}}}}$ [-].

In a superconducting magnet, it can sometimes be sufficient to only consider the turns or even apertures as lumped inductances. However, the electromagnetic effects still need to be resolved on the strand or filament level. If the calculated equivalent parameters R_{ec} and L_{ec} of the loops for an effect are very similar, one can limit the number of loops by summing them together and hence reduce the computational time significantly. Combining equation (9) of the induced current change in one equivalent loop again with the voltage $V_{\mathrm{mag},1}$ across the magnets inductance in equation (2) gives for the case of $n = 2$ (e.g. $x = 1 = a$ and $x = 2 = s$):

$$\begin{aligned} V_{\mathrm{mag},1} =& \dot{I}_{\mathrm{mag},1}L_{\mathrm{mag},1} - M_{\mathrm{ec},1,a}\frac{M_{\mathrm{ec},1,a}\dot{I}_{\mathrm{mag},1} + I_{\mathrm{ec},a}R_{\mathrm{ec},a}}{L_{\mathrm{ec},a}} \\ & - M_{\mathrm{ec},1,s}\frac{M_{\mathrm{ec},1,s}\dot{I}_{\mathrm{mag},1} + R_{\mathrm{ec},s}I_{\mathrm{ec},s}}{L_{\mathrm{ec},s}} \ [V]. \end{aligned} \tag{13}$$

Assuming that for a physical phenomenon, the calculated, equivalent parameter of the loops are rather similar, e.g. that $R_{\mathrm{ec},a} \approx R_{\mathrm{ec},s} = R'_{\mathrm{ec}}$ and $L_{\mathrm{ec},a} \approx L_{\mathrm{ec},s} = L'_{\mathrm{ec}}$, one can insert equation (9) into equation (13) and obtain:

$$\begin{aligned} V_{\mathrm{mag},1} = \dot{I}_{\mathrm{mag},1}L_{\mathrm{mag},1} - \frac{1}{L'_{\mathrm{ec}}}\Bigg[& \underbrace{(M^2_{\mathrm{ec},1,a} + M^2_{\mathrm{ec},1,s})}_{=(M'_{\mathrm{ec}})^2}\dot{I}_{\mathrm{mag},1} \\ & - R'_{\mathrm{ec}}\underbrace{(M_{\mathrm{ec},1,a}I_{\mathrm{ec},a} + I_{\mathrm{ec},s}M_{\mathrm{ec},1,s})}_{=M'_{\mathrm{ec}}I'_{\mathrm{ec}}}\Bigg] \ [V], \end{aligned} \tag{14}$$

where we identify the new summed parameters. For the general case of n loops with similar equivalent parameters R_{ec} and L_{ec}, one can approximately lump them together with the new summed parameters:

$$R'_{\mathrm{ec}} = \frac{1}{n}\sum_{i=1}^{n} R_{\mathrm{ec},i} \quad [\Omega], \tag{15}$$

$$L'_{\mathrm{ec}} = \frac{1}{n}\sum_{i=1}^{n} L_{\mathrm{ec},i} \quad [\mathrm{H}], \tag{16}$$

$$M'_{\mathrm{ec}} = \sqrt{\sum_{i=1}^{n} M^2_{\mathrm{ec},i}} \quad [\mathrm{H}], \tag{17}$$

$$I'_{\mathrm{ec}} = \frac{1}{M'_{\mathrm{ec}}}\sum_{i=1}^{n} M_{\mathrm{ec},i}I_{\mathrm{ec},i} \quad [\mathrm{A}], \tag{18}$$

where R'_{ec} and L'_{ec} are the average resistance and inductance across all summed loops. This summation is possible when, for example, the parameters R and L only depend on geometrical parameters, which are equal for the same cable. In other cases, for example, when magneto-resistivity has to be considered, the summation is no longer valid.

If the physical phenomena are coupled with each other, it is also necessary to mutually couple the inductances of the coupling loops together. This is especially necessary if the time constants τ_{ec} of the phenomena are within the same order of magnitude and if the phenomena occur within the same volumes. The derivation of the calculation of the mutual couplings between the effects will be explained in more detail in section 2.7.

The equivalent lumped-element circuit parameter for a given physical phenomenon can hence be defined solely by the power loss P_{ec}, induced current I_{ec} and a time constant τ_{ec}. In the case of a harmonic excitation in the frequency domain, one can use the convenient conversion of the time derivatives to $j\omega$ with j $(-)$ the imaginary unit and ω (s^{-1}) the circular frequency. In this case, the real part of the mutual inductance represents the attenuation (magnitude) and the imaginary part the retardation (phase shift) of the magnetic field. The derivations of those three parameters, P_{ec}, I_{ec} and τ_{ec} for the different dynamic effects are discussed in the next subsections.

2.1. Inter-strand coupling losses (ISCL)

Superconducting cables consist of a number of strands that are bundled and twisted together. A time-varying magnetic field induces currents in the strands, flowing along the strand direction and eventually closing to a loop by crossing through the so-called cross-contact resistance R_{c} $[\Omega]$ between the strands. These currents are called ISCCs [18]. In this work, only ISCC between crossing strands will be considered. Currents flowing between adjacent strands will be neglected, as the resulting losses in accelerator magnets are generally orders of magnitude smaller [18].

The power loss generated by these ISCCs in one-half of a turn can be described by [18, 21]:

$$P_{\mathrm{ISCL}} = l_{\mathrm{mag}}\beta_{\mathrm{ISCL}}w_{\mathrm{Bare}}h_{\mathrm{Bare}}\left(\frac{\mathrm{d}B_{\perp}}{\mathrm{d}t}\right)^{2} \quad [\mathrm{W}], \tag{19}$$

$$\beta_{\mathrm{ISCL}} = \frac{1}{120}\frac{L_{\mathrm{P}}}{R_{\mathrm{c}}}n_{\mathrm{S}}\left(n_{\mathrm{S}}-1\right)\frac{w_{\mathrm{Bare}}}{h_{\mathrm{Bare}}} \quad \left[\frac{\mathrm{m}}{\Omega}\right], \tag{20}$$

with l_{mag} [m] the magnetic length of the magnets' turns, w_{Bare} [m] and h_{Bare} [m] the width and height of the cable, respectively, L_{P} [m] the cable-twist pitch, n_{S} [-] the number of strands within the cable and $\left(\frac{\mathrm{d}B_{\perp}}{\mathrm{d}t}\right)$ [T A^{-1}] the total field change, perpendicular to the broad face of the cable.

For a harmonic excitation, one can easily approximate a relation for the field derivative of a given frequency and utilise the conversions to the frequency domain:

$$\left(\frac{\mathrm{d}B_{\perp}}{\mathrm{d}t}\right) = \omega f_{\mathrm{H},\perp}I_{\mathrm{Mag}}\alpha_{\mathrm{ISCL}} \quad \left[\mathrm{T\,s^{-1}}\right], \tag{21}$$

where α_{ISCL} [−] is the field attenuation and retardation factor and $f_{\mathrm{H},\perp}$ [T A^{-1}] is the perpendicular component of the magnetic transfer function f_{H} [T A^{-1}]. This function represents the generated magnetic flux density per unit of transport current in each strand-position of the magnet's coil. f_{H} can be calculated by a magneto-static simulation, for example, with ROXIE [22], and by combining the field in x- and y-directions, f_x [T A^{-1}] and f_y [T A^{-1}] respectively:

$$f_{\mathrm{H}} = \sqrt{\left(f^2{}_x + f^2{}_y\right)} \quad \left[\mathrm{T\,A^{-1}}\right]. \tag{22}$$

For ISCL, the average magnetic transfer function of all strands within the cable is used. Moreover, the field transfer function in this work was calculated in a two-dimensional model, neglecting end-effects.

In equation (21), we introduced the field attenuation and retardation factor α_{ISCL} [−], describing the relation of the phenomenon's time constant to the field attenuation. The derivation of the complex-valued α is described in detail in Annex B. Ultimately, α_{ISCL} can be expressed as:

$$\alpha_{\mathrm{ISCL}} = \gamma_{\mathrm{ISCL}}\omega\tau + j\gamma^2_{\mathrm{ISCL}} \quad [-], \tag{23}$$

$$\gamma_{\mathrm{ISCL}} = \frac{1}{\sqrt{1+\left(\omega\tau_{\mathrm{ISCL}}\right)^2}} \quad [-]. \tag{24}$$

The equivalent induced current of the ISCCs can be calculated as [21]:

$$I_{\mathrm{ISCL}} = \beta_{\mathrm{ISCL}}h_{\mathrm{Bare}}\frac{\mathrm{d}B_{\perp}}{\mathrm{d}t} \quad [\mathrm{A}]. \tag{25}$$

The time constants of the induced ISCC can vary significantly throughout the magnets' coil due to, for example, different contact pressures and the area between the cables. Moreover, if cables are stacked, their self-fields affect each other and impact the resulting ISCC and their time constants. For simplicity, we use in this work a global time constant for each cable type, assuming a uniform R_{c} between all strands and a stack of $n_{\mathrm{c}} = 15$ cables. The time constants of these coupling currents for the stack of cables are defined as [21]:

$$\tau_{\mathrm{ISCL}} = \mu_0\beta_{\mathrm{ISCL}} \quad [\mathrm{s}], \tag{26}$$

with μ_0 [H m^{-1}] the permeability of vacuum. The time constants given by equation (26) are in close agreement with time constants that were derived for a stack of cables with $n_{\mathrm{c}} = 15$ cables with a more detailed equivalent network model of ISCC [18, 21].

As described at the beginning of section 2, equations (19), (25) and (26) are sufficient to calculate the lumped-element parameters R_{ec}, L_{ec} and M_{ec} of the equivalent coupling loop.

Unlike PCs or IFCCs, ISCCs are also generated if the magnet is in the normal conducting state. In this case, the resistance of the strand along the current path of the ISCC must be considered. However, this resistance changes the current distribution of the ISCCs significantly. To still account for this type of coupling currents in the normal state, the cross-contact resistance R_{C} in equation (20) is rewritten to the contact resistance for the normal state $R_{\mathrm{C,N}}$ [Ω] and the time constant of the current loop is adjusted to fit with measurements at different temperatures. This normal state cross-contact resistance is the sum of the strands normal resistances along one twist-pitch R_{Strand} [Ω] as well as the increased cross-contact resistance between the strands $R_{\mathrm{C,Warm}}$ [Ω], and results in:

$$R_{\mathrm{C,N}} = R_{\mathrm{C,Warm}} + R_{\mathrm{Strand}} \quad [\Omega], \tag{27}$$

$$R_{\mathrm{strand}} = \rho_{\mathrm{Cu}}\frac{l_{\mathrm{P}}}{A_{\mathrm{Strand}}} \quad [\Omega], \tag{28}$$

where ρ_{Cu} [Ωm] is the resistivity of the strand's copper, l_{P} [m] the length of a strand in one twist-pitch and A_{Strand} [m^2] the area of the copper in the strand.

2.2. Eddy currents in the copper sheath

Each strand in a superconducting cable consists of a larger number of twisted superconducting filaments. These filaments are generally arranged around an inner copper core, then embedded in a copper matrix and surrounded by an outer copper sheath. An applied field change will induce eddy currents in these copper parts. The outermost region of a strand is generally the copper sheath and, hence, the first region to be penetrated by an applied field change. Due to the resistivity of copper at low frequencies, the developed eddy currents cannot significantly oppose the applied field change, thereby giving rise to the development of PCs and IFCCs. In the superconducting state and for small enough field excitations, there are no eddy currents in the copper core of the conductor, as the superconducting filaments and the developed PCs therein fully shield the field. However, with increasing frequency, the eddy currents in the outer copper sheath increasingly shield the field from the inside of the strand, reducing the development therein.

We will call these currents copper-sheath coupling currents (CSCC). As these currents flow through a resistive material,

they cause a loss, referred to as copper-sheath coupling loss (CSCL).

The power loss in the strands' copper can be calculated by assuming two frequency-dependent regimes. For this, we introduce the skin depth [23]:

$$\delta = \sqrt{\frac{2\rho_{\mathrm{Cu}}}{\omega\mu_0}} \qquad [\mathrm{m}], \tag{29}$$

with ρ_{Cu} [Ωm] the resistivity of copper in the strands outer sheath.

The first regime describes the low-frequency loss. In this regime, the skin depth of the copper is still larger than the actual thickness of the conductor, and the generated field change by the eddy currents can be assumed to be a small perturbation to the applied field change.

We assume a longitudinally induced current density following a $\cos(\theta)$ distribution in the low frequency (LF) regime of [23]:

$$J_{\mathrm{Cu,LF}}(r,\theta) = \frac{r\cos(\theta)}{2\rho_{\mathrm{Cu}}}\frac{\mathrm{d}B}{\mathrm{d}t} \quad \text{if } \delta \geqslant \left(1-\frac{1}{e}\right) r_{\mathrm{s,o}} \qquad [\mathrm{A\,m^2}], \tag{30}$$

with r and θ the polar coordinates and $r_{\mathrm{s,o}}$ [m] the outer strand radius. The induced currents generate a dipole field, opposing the applied field.

In the second regime, the skin effect within the copper must be taken into account. From any given point on the round surface of the strand, the magnetic flux decays exponentially with the skin depth. The current density in the radio frequency (RF) regime hence takes the form of [23]:

$$J_{\mathrm{Cu,RF}}(r,\theta) = \frac{r\cos(\theta)}{2\rho_{\mathrm{Cu}}}\exp\left(-\frac{r}{\delta}\right)\frac{\mathrm{d}B*}{\mathrm{d}t} \quad \text{if } \delta < \left(1-\frac{1}{e}\right) r_{\mathrm{s,o}} \qquad \left[\mathrm{A\,m^2}\right]. \tag{31}$$

The induced currents are proportional to the square of the field change:

$$\frac{\mathrm{d}B}{\mathrm{d}t} = \omega f_{\mathrm{H}} I_{\mathrm{Mag}} \alpha_{\mathrm{CSCL}} \qquad \left[\mathrm{T\,s^{-1}}\right], \tag{32}$$

$$\frac{\mathrm{d}B^*}{\mathrm{d}t} = \omega f_{\mathrm{H}} I_{\mathrm{Mag}} \qquad \left[\mathrm{T\,s^{-1}}\right], \tag{33}$$

with the field attenuation α_{CSCL} as:

$$\alpha_{\mathrm{CSCL}} = \gamma_{\mathrm{CSCL}}\omega\tau + j\gamma_{\mathrm{CSCL}}^2 \qquad [-], \tag{34}$$

$$\gamma_{\mathrm{CSCL}} = \frac{1}{\sqrt{1+(\omega\tau_{\mathrm{CSCL}})^2}} \qquad [-]. \tag{35}$$

In the second regime, the field attenuation factor is dropped, as the skin-depth dependence takes this effect into account.

The power loss associated with the eddy currents in the copper sheath can then be calculated for one strand by integrating over the volume of the conductor, and results in [24, 25]:

$$P_{\mathrm{CSCL}} = \begin{cases} d_{\mathrm{s,o}}^4 \frac{\pi}{4\rho_{\mathrm{Cu}}}\left(\frac{\mathrm{d}B}{\mathrm{d}t}\right)^2 & \text{if } \delta \geqslant \left(1-\frac{1}{e}\right) r_{\mathrm{s,o}} \\ \delta^3 \frac{\pi\, d_{\mathrm{s,o}}}{\rho_{\mathrm{Cu}}}\left(\frac{\mathrm{d}B^*}{\mathrm{d}t}\right)^2 & \text{if } \delta < \left(1-\frac{1}{e}\right) r_{\mathrm{s,o}} \end{cases} \qquad [\mathrm{W}], \tag{36}$$

where $d_{\mathrm{s,o}} = 2r_{\mathrm{s,o}} = d_{\mathrm{s}}$ [m] describes the outer diameter of the strand. The total induced current can be calculated by integrating the induced current density from the outside of the strand towards the inside and over one-half of the strand. For the sake of simplicity, we will consider only an applied field in the y-direction. The integral can then be expressed as:

$$I_{\mathrm{CSCL}} = 2\int_{-\pi/2}^{\pi/2}\int_{r_{\mathrm{s,o}}}^{0} J_{\mathrm{Cu}}(r,\theta)\,\mathrm{d}r\mathrm{d}\theta \qquad [\mathrm{A}], \tag{37}$$

whereas for other field directions, the integration bounds of θ must be adjusted. The total induced current in the low-frequency regime then equals:

$$I_{\mathrm{CSCL,LF}} = \frac{d_{\mathrm{s,o}}^3}{3\rho_{\mathrm{Cu}}}\left(\frac{\mathrm{d}B}{\mathrm{d}t}\right) \qquad [\mathrm{A}], \tag{38}$$

$$I_{\mathrm{CSCL,RF}} = \frac{\delta d_{\mathrm{s,o}}^2}{2\rho_{\mathrm{Cu}}}\left[1-\exp\left(-\frac{d_{\mathrm{s,o}}}{\delta}\right)\right]\frac{\mathrm{d}B}{\mathrm{d}t} \qquad [\mathrm{A}]. \tag{39}$$

Finally, the time constant of this eddy-current phenomenon can be calculated as outlined in [23, 24]:

$$\tau_{\mathrm{CSCL}} = \frac{\mu_0}{8}\frac{r_{\mathrm{s,o}}^2}{\rho_{\mathrm{Cu}}} \qquad [\mathrm{s}]. \tag{40}$$

If the superconductor in the strand is in normal state, the applied magnetic field change penetrates into all copper parts of the strand. The resistivity of the strands' copper ρ_{Cu} then has to be adjusted to become an effective resistivity ρ_{CSCL} to account for the presence of the superconducting filaments in the matrix. For a round strand comprising a fraction of superconductor f_{SC} [-], uniformly distributed across the copper matrix, the effective resistivity can be calculated as follows [21]:

$$\rho_{\mathrm{CSCL}} = \rho_{\mathrm{Cu}}\frac{1-f_{\mathrm{SC}}}{1+f_{\mathrm{SC}}} \qquad [\Omega\mathrm{m}], \tag{41}$$

with f_{SC} [−] the fraction of the superconductor in the strand.

The aforementioned derivation for the eddy currents in the copper parts of the strand can only be applied to round conductors with a round outer sheath. The deformation of the strands is not taken into account.

2.3. Inter-filament coupling losses (IFCLs)

The superconducting strands comprise numerous superconducting filaments that are twisted together. An applied field change induces currents in the superconducting filaments, flowing in the direction of the transport current and eventually closing through the resistive copper matrix of the strand

after approximately half a filament twist pitch. These induced currents are called IFCC and result in the generation of IFCL.

The IFCCs and IFCLs for one strand can be calculated as [18, 26, 27]:

$$I_{\mathrm{IFCL}} = \beta_{\mathrm{IFCL}} d_{\mathrm{s}} \left(\frac{\mathrm{d}B}{\mathrm{d}t}\right) \qquad [\mathrm{A}], \tag{42}$$

$$P_{\mathrm{IFCL}} = \frac{\pi}{4} d_{\mathrm{s}}^2 l_{\mathrm{mag}} \beta_{\mathrm{IFCL}} \left(\frac{\mathrm{d}B}{\mathrm{d}t}\right)^2 \qquad [\mathrm{W}], \tag{43}$$

$$\beta_{\mathrm{IFCL}} = \left(\frac{L_{\mathrm{f}}}{2\pi}\right)^2 \frac{1}{\rho_{\mathrm{eff}}} \qquad \left[\mathrm{m\,\Omega^{-1}}\right], \tag{44}$$

where L_{f} [m] is the filament twist-pitch, ρ_{eff} the effective resistivity given by equation (41) and $\left(\frac{\mathrm{d}B}{\mathrm{d}t}\right)$ describes the total field change in the strand. The total field change generating the IFCC results in:

$$\frac{\mathrm{d}B}{\mathrm{d}t} = \omega f_{\mathrm{H}} I_{\mathrm{Mag}} \alpha_{\mathrm{IFCL}} \qquad \left[\mathrm{T\,s^{-1}}\right], \tag{45}$$

where the field attenuation factor α_{IFCL} is:

$$\alpha_{\mathrm{IFCL}} = \gamma_{\mathrm{IFCL}} \omega\tau + j\gamma_{\mathrm{IFCL}}^2 \qquad [-], \tag{46}$$

$$\gamma_{\mathrm{IFCL}} = \frac{1}{\sqrt{1 + (\omega\tau_{\mathrm{IFCL}})^2}} \qquad [-]. \tag{47}$$

The characteristic time constant τ_{IFCL} of the currents can be analytically calculated as [18, 26, 27]:

$$\tau_{\mathrm{IFCL}} = \frac{\mu_0}{2} \beta_{\mathrm{IFCL}} \qquad [\mathrm{s}]. \tag{48}$$

In the case of a low field amplitude, for example, during TFM, the filaments can become perfectly diamagnetic and fully expel the interior field. In this case, the permeability must be modified to become an effective permeability [18]:

$$\mu = \mu_{\mathrm{eff}} = \mu_0 (1 - f_{\mathrm{sc}}) \qquad \left[\mathrm{H\,m^{-1}}\right]. \tag{49}$$

2.4. PCs

If a superconductor is subject to a changing magnetic field, instantaneous supercurrents are developed at the superconductor's surface, opposing the applied magnetic field. These supercurrents are also called PCs, which can remain flowing until the superconductor transitions back into the normal state. For larger filament diameters and small enough field excitations, the superconducting filaments can even become fully diamagnetic [18].

The power loss for the case of PCs is twofold: first, due to the build-up of the induced currents that persist, some energy is taken and stored within those currents. We will refer to this as P_{stored} [W]. Second, the fluxons within the superconductor are forced to move due to increasing fields. They hence can cross through resistive impurities within the superconductor, causing a loss, here referred to as magnetisation heat and described as P_{loss} [W] [28].

It can be shown that the stored power can be described as [29, 30]:

$$P_{\mathrm{stored}} = \int_V \mathbf{H} \frac{\mathrm{d}\mathbf{B}}{\mathrm{d}t} \mathrm{d}V \tag{50}$$

$$= \mu_0 \int_V \left(\mathbf{H} \frac{\mathrm{d}\mathbf{M}}{\mathrm{d}t} + \mathbf{H} \frac{\mathrm{d}\mathbf{H}}{\mathrm{d}t}\right) \mathrm{d}V \qquad [\mathrm{W}], \tag{51}$$

where $\mathbf{H}$ [$\mathrm{A\,m^{-1}}$] is the magnetic field strength, V [$\mathrm{m^3}$] the volume of the superconductor region and $\mathbf{M}$ [$\mathrm{A\,m^{-1}}$] the magnetization of the superconductor. Moreover, in equation (51), the general constitution for the magnetic flux $\mathbf{B} = \mu_0(\mathbf{H} + \mathbf{M})$ [T] was used.

The dissipated power due to the magnetisation heat can be calculated as [28, 30]:

$$P_{\mathrm{loss}} = \int_V \mathbf{M} \frac{\mathrm{d}\mathbf{B}}{\mathrm{d}t} \mathrm{d}V, \tag{52}$$

$$= \mu_0 \int_V \mathbf{M} \left(\frac{\mathrm{d}\mathbf{H}}{\mathrm{d}t} + \frac{\mathrm{d}\mathbf{M}}{\mathrm{d}t}\right) \mathrm{d}V \qquad [\mathrm{W}], \tag{53}$$

where we take, for both cases, a constant permeability across the conductor volume.

However, the derivation of the PCs follows a different approach than the other eddy-current phenomena. These currents develop instantaneously and hence do not exhibit a time constant. Moreover, the PCs also show hysteretic behaviour, e.g. they depend on the field history of the conductor. Hence, altering the presented coupling loops by replacing the lossy resistance with a current source is necessary [30]. This current source sets the equivalent current in the loop $I_{\mathrm{ec,PC}}$, depending on the magnetisation level. The schematic for such a loop, coupled to one magnet inductance, is shown in figure 3.

The equivalent current, inductance and mutual inductance for one strand can be calculated as follows [30]:

$$I_{\mathrm{ec,PC}} = M(T, B, M_{t-1}) \cdot d_{\mathrm{s}} \qquad [\mathrm{A}], \tag{54}$$

$$L_{\mathrm{ec,PC}} = \mu_0 \frac{\pi}{4} l_{\mathrm{mag}} \qquad [\mathrm{H}], \tag{55}$$

$$M_{\mathrm{ec,PC,1}} = \mu_0 \frac{\pi}{4} d_{\mathrm{s}} l_{\mathrm{mag}} f_{\mathrm{H}} \qquad [\mathrm{H}], \tag{56}$$

with $M(T, B, M_{t-1})$ [$\mathrm{A\,m^{-1}}$] the homogenised, average magnetisation within the volume of a strand. The equivalent lumped-element parameters' derivation is described in Annex A. The derivation assumes a round conductor with a uniform magnetisation across all superconducting filaments of the wire/strand. The maximum magnetisation M_{P} for a fully saturated strand can be calculated, based on the penetration field H_{P}, as [31, 32]:

$$H_{\mathrm{P}} = \frac{J_{\mathrm{C}}(T, B)\, d_{\mathrm{f}}}{\pi} \qquad \left[\mathrm{A\,m^{-1}}\right], \tag{57}$$

$$M_{\mathrm{P}} = -\frac{2}{3} H_{\mathrm{P}} f_{\mathrm{SC}} \qquad \left[\mathrm{A\,m^{-1}}\right], \tag{58}$$

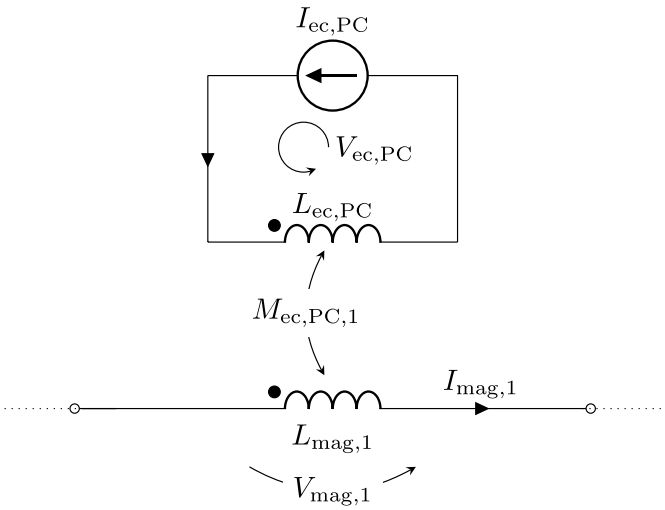

Figure 3. Equivalent lumped-element coupling loop for the persistent current effect.

with d_f [m] the diameter of the superconducting filament and $J_C(T,B)$ [A m^2] the critical current density of the superconductor. To account for the magnetisation for an arbitrary field transient, it is necessary to derive the magnetisation based on a modified version of Bean's model, for example, as presented in [30].

The magnetisation heat can be considered negligible for small field changes ΔB. Hence, the PCs flow losslessly within the superconductor. These currents would still cause a voltage change across the coil and impact the differential inductance of the magnet. The contribution can be calculated from equation (12) and setting $R_{ec} = 0$:

$$L_{Mag,D} = L_{Mag} - \frac{M_{ec,PC}^2}{L_{PC}} \tag{59}$$

$$= L_{Mag} - \mu_0 \frac{\pi}{4} d_s^2 l_{mag} f_H. \tag{60}$$

The PCs are only present while the conductor remains in the superconducting state and, hence, are set to zero in the normal state.

2.5. Eddy currents in the magnets BS

In an accelerator magnet, the beam region is generally surrounded by the magnets' BS to protect the superconducting coils from particle impacts and radiation as well as to intercept the image current power from the beam. The LHC BS is a stainless steel tube with a thin copper coating on the inside with a thickness t_{BS} [m] [33]. The generated field change during a transient in the magnet also induces eddy currents in this magnet component. The BS of the LHC main dipole is shown in figure 1.

The eddy currents and loss in the BS can be derived similarly to the eddy currents in the copper. We assume a longitudinal induced current density following a $\cos(\theta)$ distribution for the two different regimes, as presented in equations (30) and (31).

The power loss resulting from the eddy currents in the BS can then be calculated by integrating over the volume of the BS. Contrary to the eddy currents in the strands, this integration is performed over a hollow cylinder. It results in [23]:

$$P_{BS} = \begin{cases} l_{mag} \frac{\pi}{4\rho_{Cu,BS}} \left(r_{BS}^4 - (r_{BS} - t_{BS})^4 \right) \left(\frac{dB}{dt} \right)^2 \\ \text{if } \delta \geqslant \left(1 - \frac{1}{e}\right) t_{BS} \\ l_{mag} \delta^3 \frac{\pi r_{BS}}{\rho_{Cu,BS}} \left(\frac{dB^*}{dt} \right)^2 \\ \text{if } \delta < \left(1 - \frac{1}{e}\right) t_{BS} \end{cases} \quad [\text{W}], \tag{61}$$

with $\rho_{Cu,BS}$ [Ωm] the resistivity of the BSs copper layer, r_{BS} [m] the outer radius of the BS and δ the skin-depth introduced in equation (29). Note that the field change is considered differently in the two regimes:

$$\frac{dB}{dt} = \omega f_M \alpha_{BS} \qquad \left[\text{T s}^{-1}\right], \tag{62}$$

$$\frac{dB^*}{dt} = \omega f_M \qquad \left[\text{T s}^{-1}\right], \tag{63}$$

where f_M describes the magnetic transfer function in the BS region. A uniform magnetic transfer function for the whole BS can be assumed in the case of a dipole. However, this is generally not true for other multipole magnets.

The total induced current can be calculated by integrating the induced current density of one half of the BS from the outside towards the inside. For example, for an applied field in the y-direction, the integral equals:

$$I_{BS} = 2 \int_{-\pi/2}^{\pi/2} \int_{r_{BS}}^{r_{BS} - t_{BS}} J_{BS}(r,\theta)\, dr d\theta \qquad [\text{A}], \tag{64}$$

where the integration bounds need to be adjusted for other field directions. The total induced current in the low-frequency regime then follows:

$$I_{BS} = 2 \frac{t_{BS}}{3\rho_{Cu,BS}} \left(t_{BS}^2 - 3 t_{Cu} r_{BS} + 3 r_{BS}^2 \right) \left(\frac{dB}{dt} \right) \qquad [\text{A}], \tag{65}$$

and a significantly more complex term for the induced current in the high-frequency regime can be derived.

The time constant for the eddy currents in the BS can be calculated as [23]:

$$\tau_{BS} = \mu_0 \frac{r_{BS} t_{BS}}{2\rho_{Cu,BS}} \qquad [\text{s}]. \tag{66}$$

The derivation of the power loss in the BS assumes a round geometry. This is generally not true for BSs in the LHC. However, an equivalent radius can be calculated as, for example, presented in [34].

Moreover, the manufacturing process of the BS causes a chemical diffusion of stainless steel particles into the copper and can hence deteriorate the purity of the copper layer [35]. For a more sophisticated model of the eddy currents in the BS multiple layers need to be taken into account, for example, one

layer for the high-purity inner part, one layer for the deteriorated copper and one layer for the eddy currents in the stainless-steel part of the BS. We will refer to these layers as the BS's inner and outer copper layers, respectively. Due to the complexity of the derivation, it is not presented in this work, but a similar approach can be found, for example, in [25].

2.6. Eddy currents in the W, CB and CPSs

Besides the BS, the magnet also includes other components made of low-resistivity materials. The CB, made of stainless steel, separates the inner beam- and vacuum region from the superconducting coils. In the case of cos-theta-type accelerator magnets, the different coil blocks are generally separated from each other by coil W of various shapes and sizes, which can be made of copper. Moreover, the superconducting coils can sometimes be covered for manufacturing reasons with CPSs, which can also be made of a low-resistivity material [36].

Generally, these magnet components have a rather complex geometry, and an analytical derivation becomes quickly unfeasible. However, in specific frequency regimes, the developed eddy currents can still majorly impact the magnets' impedance. A consecutive simulation approach was chosen to account for the eddy currents in these magnet components. First, the electromagnetic effect of the magnet components is simulated in 2D utilising FEM, for example, COMSOL Multiphysics©. In these simulations, the magnet coils carry a uniform current density, oscillating at a given frequency. Afterwards, the frequency-dependent eddy currents, power loss within the resistive magnet components, and time constants are exported to calculate the equivalent parameters for the coupling loops in the network model.

2.7. Coupling of effects

The described dynamic effects are tightly coupled with each other and very interdependent. We will distinguish, in general, two types of coupling: external and internal coupling.

The inductance matrix used in this model is shown in figure 4 with the loop inductances on the diagonal and the mutual couplings to all other equivalent loops off-diagonal and with the different types of coupling indicated in colours. The mutual inductances are named with the first subscript defining the cause e.g. $M_{\mathrm{ISCC,CSCC}}$ describing the effect of the ISCC on the CSCC.

The inductance matrix is, by definition, symmetric. This implies that it is sufficient to derive the mutual couplings between two effects in one direction, e.g. deriving the impact of one effect on the other. Conveniently, the respective other direction does not have to be calculated. These couplings which are not resolved are marked in figure 4 in grey.

2.7.1. Internal coupling. Internal coupling describes the interdependence between the effects if they are generated within the same volume. In this case, the effects can be directly coupled with their field attenuation factors.

The field attenuation factor for the IFCL α_{IFCL} can hence be rewritten by combining the effects of the IFCL and the CSCL in an equivalent time constant [24]:

$$\alpha^{*}_{\mathrm{IFCL}} = \gamma_{\mathrm{IFCL}}\omega\tau + j\gamma^{2}_{\mathrm{IFCL}} \qquad [-], \tag{67}$$

$$\gamma_{\mathrm{IFCL}} = \frac{1}{\sqrt{1+\left(\omega\left(\tau_{\mathrm{IFCL}}+\tau_{\mathrm{CSCL}}\right)\right)^{2}}} \qquad [-]. \tag{68}$$

Utilising the field attenuation factor $\alpha^{*}_{\mathrm{IFCL}}$ in equation (45), one can derive the IFCC and IFCL, including the effect of the CSCL.

However, as the PCs exhibit no time constant, the couplings between PC and IFCL/CSCL must be derived analytically. The mutual coupling between the two respective coupling loops can be calculated similarly, as shown in Annex A, by deriving the equivalent network power and comparing it to the equations for the physical power loss. The analytical formula results in [30]:

$$M_{\mathrm{IFCL,PC}} = M_{\mathrm{CSCL,PC}} = \mu_0 \frac{\pi}{8} l_{\mathrm{mag}} \qquad [\mathrm{H}]. \tag{69}$$

2.7.2. External coupling. External coupling describes the interdependence between the effects if these are not generated within the same volume. The eddy currents of the effects create a field change on their own in their vicinity, which can affect the eddy currents in another volume.

To take the effect of the inter-strand coupling currents onto PC, IFCL and CSCL into account, one has to calculate the field generated by the ISCC B_{ISCL}, attenuating the applied field inside the cable. For the case of a Rutherford cable, as shown in figure 5, this generated return field is approximated in this work by assuming the ISCC as current lines on each side of the cable's broad face and calculated with Biot–Savart's law:

$$B_{\mathrm{ISCL}} = \mu_0 \frac{I_{\mathrm{ISCL}}}{4\pi}\frac{1}{r} \qquad [\mathrm{T}], \tag{70}$$

where r [m] describes the distance between each strand and the respective current lines. The total field generated in a single strand by the ISCC is, therefore, the sum of the fields generated by the two current lines. The return field of the ISCC opposes the perpendicular applied field on the cables and causes an attenuation of the field seen by all strands inside the cable. Decomposing B_{ISCL} into its x- and y- components provides the new magnetic transfer function coefficient $f_{\mathrm{H}}{}^{*}$ [T A^{-1}]. Using f^{*}_{H} in the derivation of the power-loss and induced currents hence includes the effect of the ISCL. The effect of the generated field of the ISCC on the ISCC in neighbouring cables is not considered. However, such coupling could be included by implementing a more detailed field calculation.

For the mutual coupling of the magnets components and the conductor losses, FEM is used. The magnetic transfer function in each strand position is calculated for all frequencies and

L_{ISCC}	$M_{\mathrm{ISCC,CSCC}}$	$M_{\mathrm{ISCC,IFCC}}$	$M_{\mathrm{ISCC,PC}}$	$M_{\mathrm{ISCC,BS}}$	$M_{\mathrm{ISCC,W}}$	$M_{\mathrm{ISCC,CPS}}$	$M_{\mathrm{ISCC,CB}}$
$M_{\mathrm{CSCC,ISCC}}$	L_{CSCC}	$M_{\mathrm{CSCC,IFCC}}$	$M_{\mathrm{CSCC,PC}}$	$M_{\mathrm{CSCC,BS}}$	$M_{\mathrm{CSCC,W}}$	$M_{\mathrm{CSCC,CPS}}$	$M_{\mathrm{CSCC,CB}}$
$M_{\mathrm{IFCC,ISCC}}$	$M_{\mathrm{IFCC,CSCC}}$	L_{IFCC}	$M_{\mathrm{IFCC,PC}}$	$M_{\mathrm{IFCC,BS}}$	$M_{\mathrm{IFCC,W}}$	$M_{\mathrm{IFCC,CPS}}$	$M_{\mathrm{IFCC,CB}}$
$M_{\mathrm{PC,ISCC}}$	$M_{\mathrm{PC,CSCC}}$	$M_{\mathrm{PC,IFCC}}$	L_{PC}	$M_{\mathrm{PC,BS}}$	$M_{\mathrm{PC,W}}$	$M_{\mathrm{PC,CPS}}$	$M_{\mathrm{PC,CB}}$
$M_{\mathrm{BS,ISCC}}$	$M_{\mathrm{BS,CSCC}}$	$M_{\mathrm{BS,IFCC}}$	$M_{\mathrm{BS,PC}}$	L_{BS}	$M_{\mathrm{BS,W}}$	$M_{\mathrm{BS,CPS}}$	$M_{\mathrm{BS,CB}}$
$M_{\mathrm{W,ISCC}}$	$M_{\mathrm{W,CSCC}}$	$M_{\mathrm{W,IFCC}}$	$M_{\mathrm{W,PC}}$	$M_{\mathrm{W,BS}}$	L_{W}	$M_{\mathrm{W,CPS}}$	$M_{\mathrm{W,CB}}$
$M_{\mathrm{CPS,ISCC}}$	$M_{\mathrm{CPS,CSCC}}$	$M_{\mathrm{CPS,IFCC}}$	$M_{\mathrm{CPS,PC}}$	$M_{\mathrm{CPS,BS}}$	$M_{\mathrm{CPS,W}}$	L_{CPS}	$M_{\mathrm{CPS,CB}}$
$M_{\mathrm{CB,ISCC}}$	$M_{\mathrm{CB,CSCC}}$	$M_{\mathrm{CB,IFCC}}$	$M_{\mathrm{CB,PC}}$	$M_{\mathrm{CB,BS}}$	$M_{\mathrm{CB,W}}$	$M_{\mathrm{CB,CPS}}$	L_{CB}

Figure 4. Inductance matrix of the equivalent effect loops in the coupled lumped-element network, with the respective loop inductance ( ) on the diagonal and the couplings to all other loops off-diagonal. The colours indicate the type of coupling: internal coupling ( ), external coupling based fully on analytical equations ( ), external coupling based on a field factor calculated in FEM and included in analytical equations ( ) and external coupling based on fully FEM ( ). Couplings which are not resolved due to symmetry are indicated with ( ).

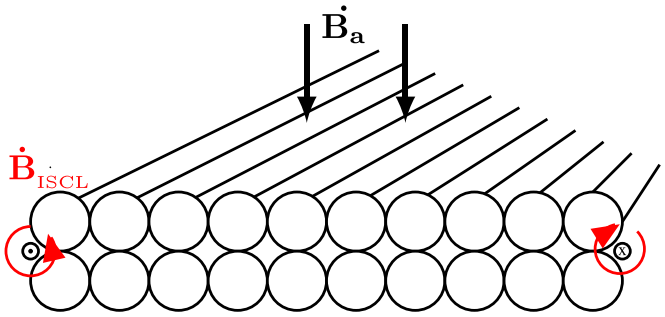

Figure 5. The return effect of the ISCL on the applied field change $\dot{\mathbf{B}}_a$ is modelled with current lines in the centre of the cable's broad face sides, carrying the calculated, equivalent I_{ISCL} and generating the field change $\dot{\mathbf{B}}_{\mathrm{ISCL}}$, opposing, therefore, the applied field change.

then used for the calculation of the respective power loss and induced current, instead of the magnetic transfer function from the magneto-static simulation.

Mutual coupling between the magnet components is also calculated utilising FEM. For these simulations, one component is excited with an oscillating current, and by extracting the induced current and power loss within the other component, the mutual coupling between these components can be calculated as defined in equation (6).

2.7.3. Derivation of mutual coupling. To calculate the mutual coupling between two loops, one can calculate the analytically derived parameters of the loop for the coupled case as described above in sections 2.7.1 and 2.7.2 and compare them to the ones in the physically uncoupled case (as derived in sections 2.1–2.6). The voltage across the magnet inductance for the first case and for the second case, in which an equivalent coupling between the loops is inserted, have to be equal.

Referring to figure 2 and assuming that there is no coupling element between the two coupling loops, the magnet voltage is defined as in equation (13). Inserting a mutual coupling between loops a and s, we obtain a voltage across the magnet inductance of:

$$\begin{aligned} V_{\mathrm{mag},1} =& \dot{I}_{\mathrm{mag},1} L_{\mathrm{mag},1} \\ &- M^*_{\mathrm{ec},1,a} \frac{M^*_{\mathrm{ec},1,a}\dot{I}_{\mathrm{mag},1} + I^*_{\mathrm{ec},a} R_{\mathrm{ec},a} + \dot{I}^*_{\mathrm{ec},s} M_{\mathrm{ec},a,s}}{L_{\mathrm{ec},a}} \\ &- M^*_{\mathrm{ec},1,s} \frac{M^*_{\mathrm{ec},1,s}\dot{I}_{\mathrm{mag},1} + R_{\mathrm{ec},s} I^*_{\mathrm{ec},s} + \dot{I}^*_{\mathrm{ec},a} M_{\mathrm{ec},a,s}}{L_{\mathrm{ec},s}} \quad [V], \end{aligned} \tag{71}$$

where $M^*_{\mathrm{ec},1,a}$, $M^*_{\mathrm{ec},1,s}$ and $I^*_{\mathrm{ec},s}$,$I^*_{\mathrm{ec},a}$ represent the derived equivalent mutual coupling and induced currents for the physically uncoupled case, respectively. It can be shown that the other two equivalent parameters R_{ec} and L_{ec} are independent of the coupling, as those purely depend on geometric and material parameters.

As the voltage for the uncoupled case, including the physical coupling in the derived parameters, and the voltage for the coupled case, with derived parameters assuming no coupling, are supposed to be the same, we can set equations (13) and (71) equal. One can derive the desired mutual inductance between the loops by comparing the second term, representing the effect of one of the two loops on the magnets' voltage:

$$\begin{aligned} & M_{\mathrm{ec},1,a} \frac{M_{\mathrm{ec},1,a}\dot{I}_{\mathrm{mag},1} + M_{\mathrm{ec},1,a} I_{\mathrm{ec},a} R_{\mathrm{ec},a}}{L_{\mathrm{ec},a}} \\ &= M^*_{\mathrm{ec},1,a} \frac{M^*_{\mathrm{ec},1,a}\dot{I}_{\mathrm{mag},1} + M^*_{\mathrm{ec},1,a} I^*_{\mathrm{ec},a} R_{\mathrm{ec},a} + \dot{I}^*_{\mathrm{ec},s} M_{\mathrm{ec},a,s}}{L_{\mathrm{ec},a}} \quad [\mathrm{V}], \end{aligned} \tag{72}$$

and the mutual inductance between the two coupling loops can be calculated as:

$$\begin{aligned} M_{\mathrm{ec},a,s} = \frac{1}{\dot{I}_{\mathrm{ec},s} M^*_{\mathrm{ec},1,a}} \Big[& \dot{I}_{\mathrm{mag},1} \left((M_{\mathrm{ec},1,a})^2 - \left(M^*_{\mathrm{ec},1,a}\right)^2 \right) \\ & + R_{\mathrm{ec},a} \left(M_{\mathrm{ec},1,a} I_{\mathrm{ec},a} - M^*_{\mathrm{ec},1,a} I^*_{\mathrm{ec},a} \right) \Big] \ [\mathrm{H}]. \end{aligned} \tag{73}$$

3. Model validation

To simulate and model the impact of non-conformities, such as short circuits, it is crucial to trust the model and to explore to which extent the model assumptions hold. Therefore, an extensive validation of the model was conducted on a wide range of available measurement data for the case of the LHC main dipole magnet. Section 3.1 describes the LHC main dipole, followed by the validation of its equivalent network in the frequency domain by measurements in section 3.2. Afterward, in section 3.3, the LHC main dipole circuit and the validation in the time domain are presented.

All simulations are performed with the SPICE solver XYCE [37], utilizing the lumped-element network described in section 2 and exemplary shown in figure 2. In the model validation, we focus on the impedance magnitude, as it is easier to interpret and visualize.

3.1. The LHC main dipole magnet

The LHC superconducting main dipole magnet consists of two apertures electrically connected in series with a total nominal inductance of $L_{\text{nom}} = 98\,\text{mH}$, operating at a temperature of $T_{\text{Op}} = 1.9\,\text{K}$ and with a nominal operating current of $I_{\text{nom}} = 11.85\,\text{kA}$, generating a nominal magnetic flux density of about $B_{\text{nom}} = 8.33\,\text{T}$. The magnet has a magnetic length of $l_{\text{mag}} = 14.3\,\text{m}$, and the coils are wound in two layers (referred to as inner and outer layer), each with a different Nb–Ti Rutherford cable. The Nb–Ti cable shows zero loss while carrying a DC current at a temperature below the current-sharing temperature. The main conductor parameters used in this work are shown in table 1.

All LHC main dipoles were assembled by three different manufacturers. The coil blocks are separated from each other with 14.3 m long copper coil W. The coil protection sheets for the main dipole are made of different materials, depending on the manufacturer. The cold bore is a stainless steel tube with an outer radius of 2.7 cm and a thickness of 1.5 mm [36]. A cross-section of the main dipole with all considered magnet components is shown in figure 1 [17].], whereas refer to table 2 for the main parameters of these magnet components. Eddy currents in other magnet components, such as in the collars or in the iron yoke, are neglected, as these elements are laminated and hence do not give rise to large loops of induced currents. Hysteresis in the iron yoke of the magnet is also neglected in this work. The power loss due to hysteresis is proportional to the area spanned by the hysteresis curve. For small field amplitudes and hence asymmetric loops, this area is negligible [41]. FEM simulations, utilising a modified Jiles-Atherton model [42] in COMSOL Multiphysics©, showed that the hysteresis power loss at all frequencies remains multiple orders of magnitude smaller than in other components. Figure 6 shows the magnetic flux density generated in the coils and magnet components for an excitation current of 1 A.

The measurement set-up for the TFM is shown in figure 7 [17]. The magnet is excited with a voltage of $V_{\text{AC}} = 10\,\text{V}$. The impedance is calculated from the measured current in the reference resistor $R_{\text{Ref}} = 25\,\Omega$ and the voltage across the magnet, and reads

$$\mathbf{Z} = \frac{\mathbf{V_{DUT}}}{\mathbf{V_{Ref}}} \cdot R_{\text{Ref}} \qquad [\Omega]. \tag{74}$$

The size of reference resistor was chosen to ensure a good signal-to-noise ratio and to limit the current to ensure safe operation via the sensitive voltage taps. In the LHC, each dipole has a parallel resistor $R_{\text{Par}} = 100\,\Omega$. Such a resistor can be included in stand-alone measurements to recreate the conditions in the LHC. All simulations use the network model shown in figure 7 in which the magnet part is replaced with the model shown in figure 2.

The stray capacitance to ground used in the simulation was adapted to the measured value of both apertures of $C_{\text{GND}} \approx 300\,\text{nF}$.

Table 1. Assumed main conductor parameters of the LHC main dipole [36, 38–40].

Parameter	Unit	Inner layer	Outer layer
Cable cross-section	mm^2	31.2	24.8
Number of strands	—	28	36
Copper/Nb-Ti	—	1.65	1.95
Strand diameter	mm	1.065	0.825
Diameter filament region	mm	0.88	0.66
Strand twist pitch	mm	115	100
Cross-contact resistance	$\mu\Omega$	50	
Filament twist pitch	mm	18	15
Filament diameter d_{f}	μm	7	6
RRR of copper	—	190	

Table 2. Main parameters of the magnets components [36, 38].

Component	Cross-section [m^2]	Material	Assumed ρ at 1.9 K [nΩm]
Cold-bore	$2.38 \cdot 10^{-4}$	316 LN Steel	650
Copper wedges	$1.15 \cdot 10^{-3}$	OF copper C106	0.54
CPS 1	$2.59 \cdot 10^{-4}$	$CuSn_3Zn_9$	60
CPS 2		$CuSn_9P$	107
CPS 3		$Cu_{61}Ni_{18}Zn_{20}$	220
CPS 4		YUS 130S Steel	640

3.2. Validation of frequency measurements

3.2.1. Stand-alone main dipole in CERN magnet test facility. A stand-alone LHC main dipole was recently cooled down in the CERN magnet test facility, and an extensive

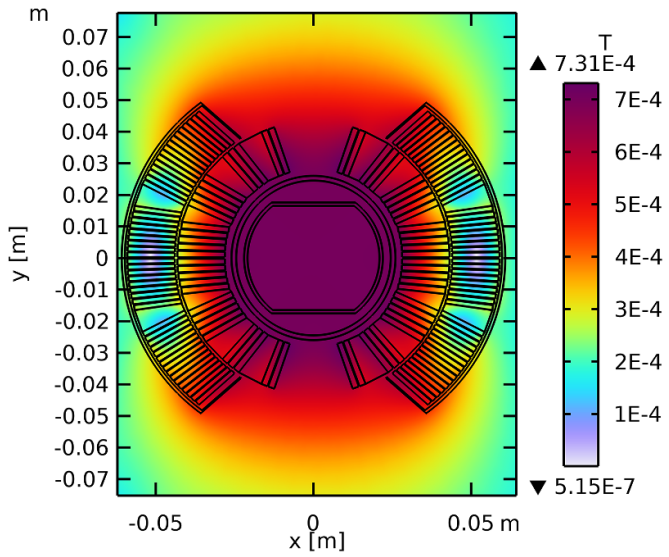

Figure 6. Magnetic field B_a within the coil and magnet components of the main dipole magnet for an excitation of 1 A, simulated with COMSOL Multiphysics© and [20].

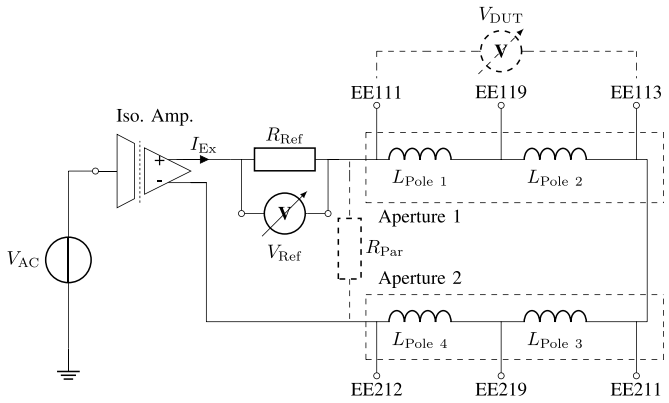

Figure 7. Schematic showing the measurement set-up. The impedances are measured across various voltage taps (here shown for aperture 1). Figure taken from [17].

TFM campaign was performed [17]. The impedance of the magnet without a transport current in the frequency range of 1 Hz to 100 kHz was measured at different temperatures and magnetisation states. A BS was not present during these measurements. The measurement campaign and set-up are described in more detail in [17] as well as the validation up to a few kHz.

The full TFM, in comparison to the simulation results from the equivalent network model, is shown in figure 8 for the case with and without a parallel resistor R_{Par}. One can observe a good agreement between the simulation and the measurement throughout the frequency range up to 20 kHz with an average error between 4.3% and 4.5%. The maximum error between the simulation and the measurement up to a frequency of 20 kHz is 7% and 12% for the case without and with the parallel resistor, respectively. Compared to an ideal inductor and

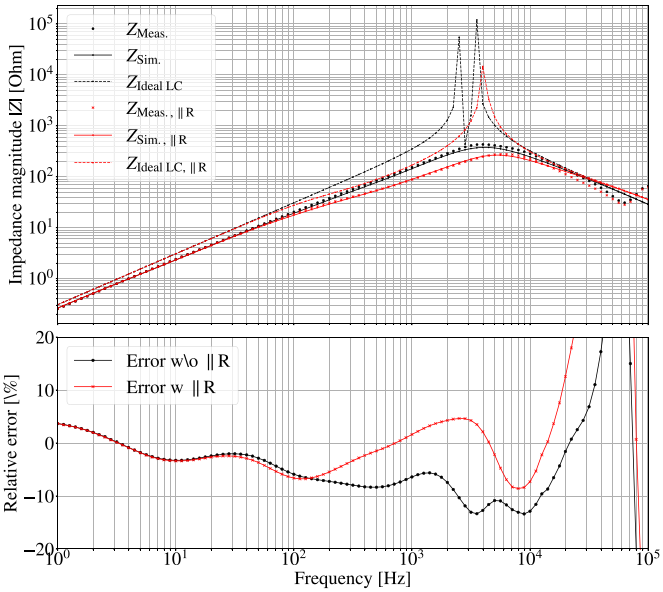

Figure 8. Measured complex impedance of one aperture of the LHC main dipole magnet versus the simulated impedance of the equivalent network model for the full measurement range at 1.9 K. The measurements with and without a parallel resistor $R_{Par} = 100\,\Omega$ are compared to the respective simulations of the model and simulations, assuming an ideal inductance and capacitance.

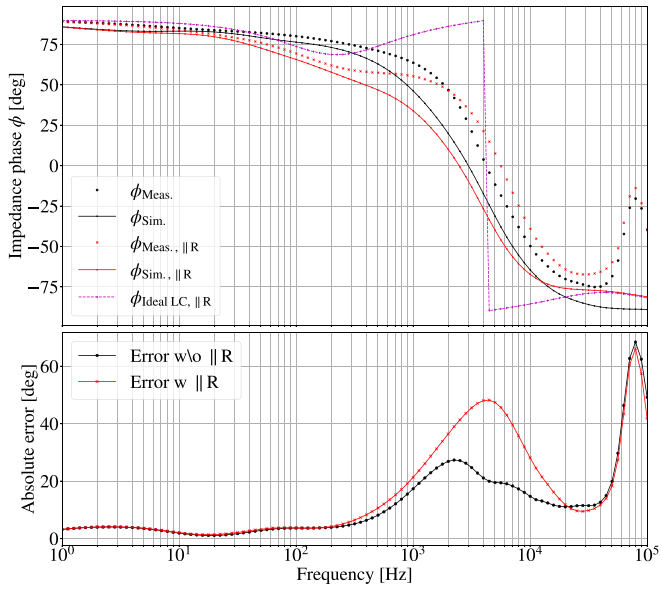

Figure 9. Measured impedance phase of one aperture of the LHC main dipole magnet versus the simulated phase of the equivalent network model for the full measurement range at 1.9 K. The measurements with and without a parallel resistor $R_{Par} = 100\,\Omega$ are compared to the respective simulations of the model and simulations, assuming an ideal inductance and capacitance.

capacitance to ground, the simulations show an average error of more than 150% and a maximum error far beyond 500%. Figure 9 shows the comparison of the measured and simulated phase for the two cases and the ideal LC network. At lower

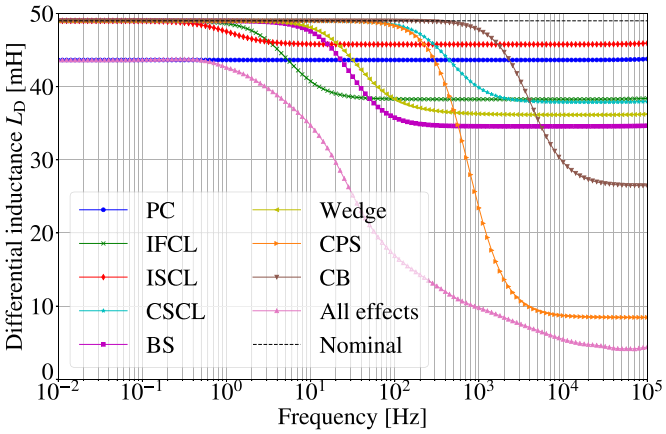

Figure 10. Impact of the different effects on the differential inductance $L_{\mathrm{mag,D}}$ of one aperture of the LHC main dipole as a function of the frequency. In this illustration, the coupling between the different effects is only considered for the curve, including all effects.

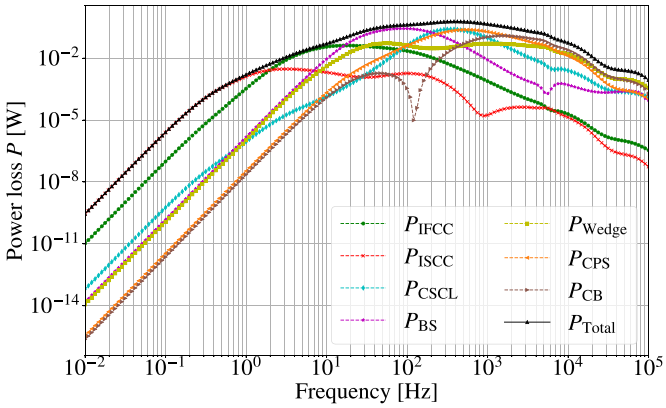

Figure 11. RMS power loss due to the different, coupled effects in one aperture of the LHC main dipole, assuming a sinusoidal excitation of $V_{\mathrm{Ex}} = 10\,\mathrm{V}$ across the magnet and a reference resistor $R_{\mathrm{Ref}} = 25\,\Omega$.

frequencies, the simulated and measured phases show good agreement. Around the resonance peak, the measured phase seems to drop later, leading to a more significant absolute error. The general shape of the phase over the frequency range is, however, captured in good agreement. Except for the BS, the simulations include all described non-linear, frequency-dependent effects. One must note that the parameters shown in tables 1 and 2, were not specifically fitted to the measurements. Further optimisation of those parameters could potentially reduce the error even further. However, fitting the model parameters to one specific magnet is not within the scope of this work.

The contributions of the different effects on the impedance and the magnets' differential inductance can be seen for one aperture in figure 10. One has to note that only the differential inductance, including all effects, shown in figure 10, does account for the coupling between the different effects. The PCs in the superconductor develop immediately and alter the differential inductance of the magnet throughout the entire frequency range. The other effects start to reduce the differential inductance at specific frequencies, which roughly correspond to the inverse of their time constants, as will be shown later. Moreover, figure 10 also shows in which frequency regimes which effect has the most significant contributions to the differential inductance. While the effects in the conductor volume mainly affect the differential inductance at lower frequencies, the effects in the magnet components are dominant at higher frequencies.

The dissipated power due to the different effects, assuming the measurement set-up used for the TFM is shown in figure 11. The root mean square power loss shown in figure 11 is based on the complex voltage and current in the equivalent loop of the network model and calculated as:

$$P = \frac{1}{2}\Re\left\{\mathbf{U_R}\cdot\bar{\mathbf{I}}_{\mathbf{Loop}}\right\} \qquad [\mathrm{W}], \tag{75}$$

where U_{R} [V] is the voltage across the resistance in the equivalent loop and $\bar{I}_{\mathrm{Loop}}$ [A] is the complex conjugate of the current flowing in the loop. These losses also consider the individual coupling between the different effects. One can observe the frequency regimes in which specific effects dominate. In the LF range up to about $\approx$100 Hz the power is mostly dissipated in the conductor. At higher frequency regimes, the eddy current losses in the magnet components become dominant. However, due to the coupling between the effects, the rise of eddy currents and their loss in one component can cause a decrease in another component. This can be observed, for example, when the power in the cold bore suddenly decreases once the power loss in the strongly coupled BS decreases.

To highlight the importance of the mutual coupling between the different effects, figure 12 compares measured impedance and simulated impedance, with and without considering coupling between the effects in the lumped element network.

One can observe that by not including the coupling, the error with respect to the measurement becomes significantly larger, up to a factor of three. The impedance simulated without the coupling generally gives a smaller impedance at lower frequencies, as it overestimates the effect of the conductor losses. On the contrary, at higher frequencies, it gives a larger impedance, as the field change generated by some components can increase the generation of currents. In the LHC main dipole, this is especially the case for the interdependence of the eddy currents in the W and ISCC. The currents in the W tilt the field so that the perpendicular field component to the cables' broad face increases.

The complex impedance of the main dipole was also monitored during the warm-up from 1.9 K to room temperature. The measured complex impedance of the stand-alone dipole for a few selected temperatures is shown in figure 13 and the assumed material resistivites in the considered components at these temperatures are shown in table 3. The complex impedance shows multiple temperature-dependent effects

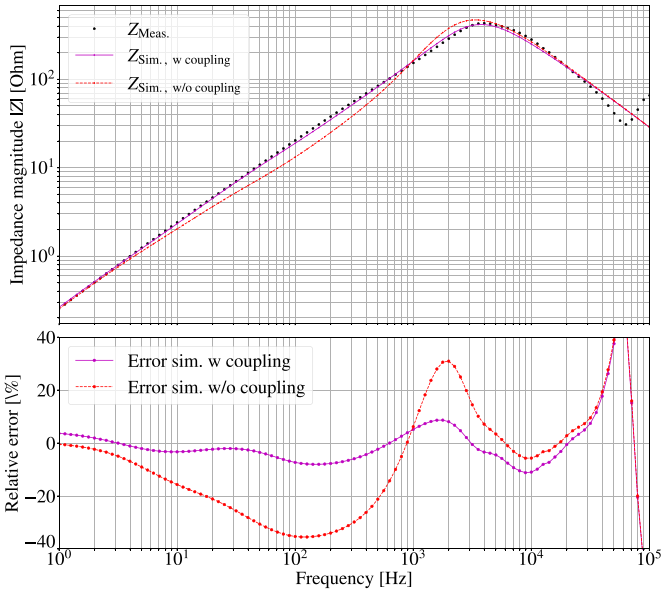

Figure 12. Measured complex impedance of one aperture of the LHC main dipole magnet versus the simulated impedance of the equivalent network model with and without considering coupling between the different equivalent coupling loops.

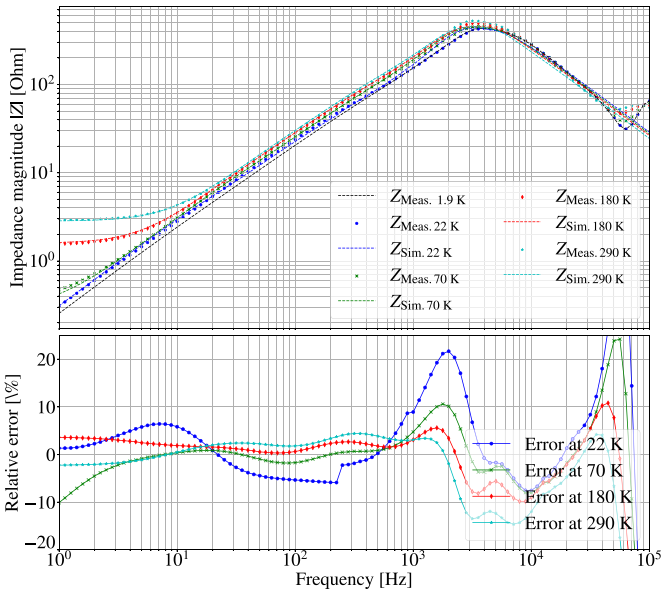

Figure 13. Measured complex impedance of one aperture of the LHC main dipole versus the simulated impedance of the equivalent network model for a few selected temperatures during the warm-up in CERN's magnet test facility.

accurately captured in the model. First, one can observe a jump in impedance at low frequencies between the measurements at the superconducting state at 1.9 K and the normal state at 22 K. The measured inductance and capacitance as a function of temperature can be seen in [17]. A sudden jump of the differential inductance was observed around ≈9.2 K, which can be accurately reproduced by the simulations, including the effects of the PCs. Beyond 9.2 K, the conductors of the main dipole are not superconducting anymore and, hence, do not show any

Table 3. Assumed material resistivities at different temperatures.

Resistivities (nΩm)	$\rho_{22\,\mathrm{K}}$	$\rho_{70\,\mathrm{K}}$	$\rho_{180\,\mathrm{K}}$	$\rho_{290\,\mathrm{K}}$
316 LN Steel (CB)	505	530	600	680
YUS 130S Steel (CPS)	640	680	820	930
Copper, RRR = 15 (Wedge)	1	3	10	18

persistent or IFCCs. However, ISCL and eddy currents in the strands' copper still alter the magnet's differential inductance.

In the normal state, the magnet's resistive behaviour becomes more dominant with a rising temperature. One can see that the warm resistances of the cables, assuming the mentioned RRR, are accurately reproduced. However, the inductive behaviour becomes dominant at frequencies above roughly 20 Hz. Up to about 300 Hz, one can observe little differences between the different temperatures as the non-linear effects present in the normal state only have a small impact on the differential inductance. At frequencies above 300 Hz, the effects of ISCL and CSCL become visible and are in good agreement with the measurements.

The time constants of the effects are presented in table 4 and shown in figure 14 as a function of the temperature.

The time constants in the superconducting state are inversely related to the differential inductance drops due to the effects, shown in figure 10, and can also be observed in figure 11. Once the conductors transition into the normal state, the time constant of the ISCL drops significantly as these currents flow now within the copper matrix of the strands along the direction of the transport current. On the contrary, the time constant of the eddy currents in the copper matrix increases after the transition, as in the normal state, no PCs develop, which shields the field change from the inner copper core of the superconducting strand. Both phenomena, as well as the eddy currents in the BS and the copper W, depend on the resistivity of the copper and hence are monotonously decreasing with the temperature. The time constants of the magnet components, made of materials other than copper, have a very small RRR, and hence, their time constants are not significantly changing with temperature.

3.2.2. Measurements of main dipole magnets installed in the LHC. Contrary to the presented stand-alone magnet in the test facility, the magnets installed in the LHC do contain a BS in the centre of each aperture, which has a significant impact on the magnet's impedance (see figure 10). Moreover, the dipole magnets in the LHC were manufactured by different companies that used four different materials for the CPSs (see table 2). All these features are included in the equivalent network model. Figure 15 compares the impedance measurement of one magnet chosen from each group of CPSs and the respective simulations. The different materials used for the CPS cause a significant difference in the impedance that can reach even up to a factor of 5 at frequencies above roughly 300 Hz. Moreover, these effects also govern the frequency at which the impedance peaks. These can vary between

Table 4. Time constants of the considered effects at 1.9 K.

	τ_{PC}	τ_{ISCL}	τ_{IFCL}	τ_{BS}	τ_{W}	τ_{CSCL}	τ_{CPS}	τ_{CB}
(ms)	—	269 (outer) 144 (inner)	23 (outer) 33 (inner)	5.8	4.5	0.34 (outer) 0.56 (inner)	0.07	0.046

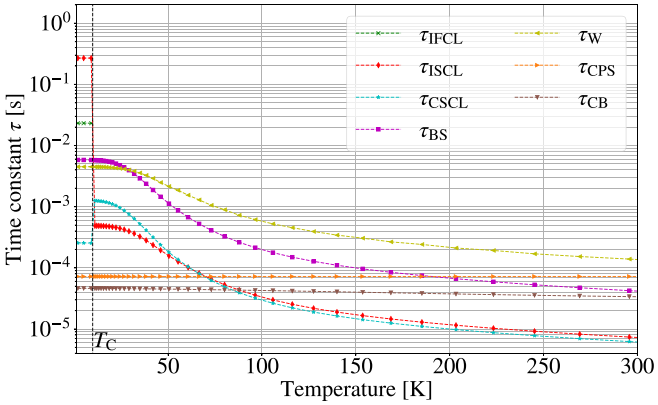

Figure 14. Calculated time constants of the equivalent lumped-element loops, representing the lossy eddy-current effects, as a function of the temperature. Time constants are assumed not to be frequency-dependent.

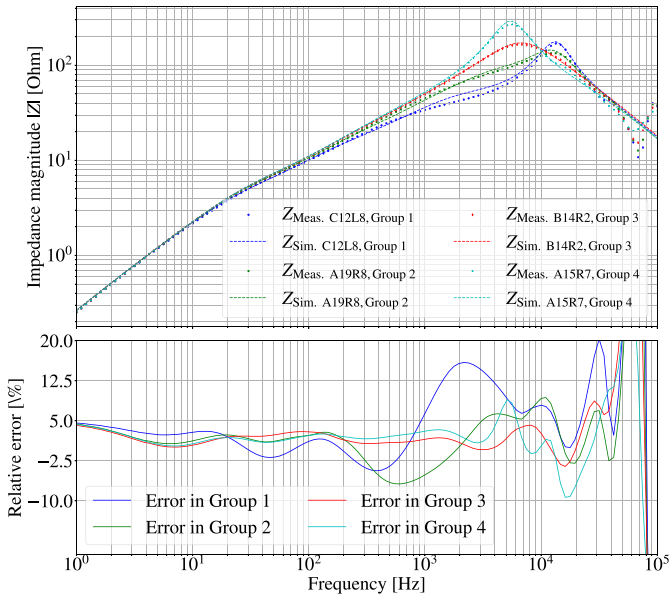

Figure 15. Comparison of complex impedance measurements of one aperture of four different LHC main dipoles installed in the LHC and the simulation results, utilising the equivalent network model. The groups refer to the used CPS materials in table 2.

about 5.5 kHz (Group 4) to 10.5 kHz (Group 1). The agreement between the measurements and the simulated impedance is very good across all groups and the entire frequency range. The average error between simulation and measurement ranges between about 1% (Group 3) and 4.5% (Group 1), with the largest deviation in Group 1 of about 17%. The model also accurately captures the effect of the BS, the different materials

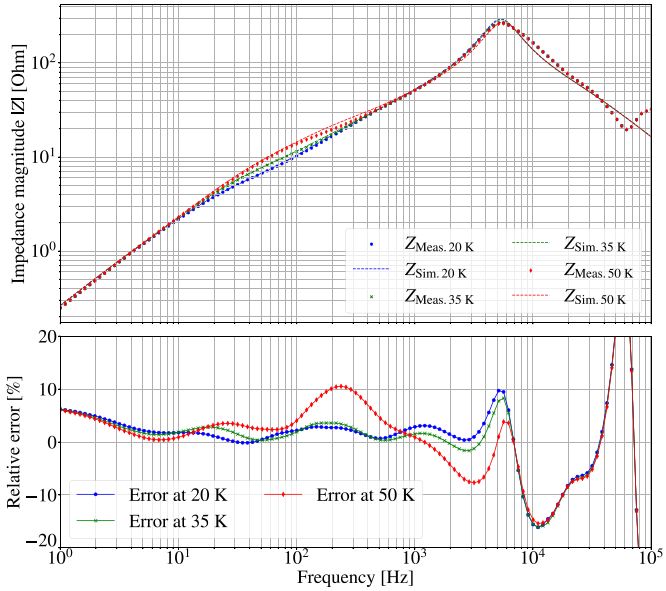

Figure 16. Comparison of complex impedance measurements of one aperture of one LHC main dipole at different temperatures of the beam-screen and the simulation results.

of the CPSs, and the interdependence of these magnet components with the conductor effects.

Additional measurements were performed to validate the model further and, specifically, the effect of the BS on the magnet's impedance. During these measurements, a set of magnets installed in the LHC was kept at their operational temperature of 1.9 K, while their BSs were heated up from the nominal temperature of 20 K to 35 K and to 50 K. The complex impedance was measured at these three temperatures. The results of these measurements for one chosen magnet are shown in figure 16. The BS model includes three different layers. The inner layer is assumed to be high-purity copper, which was not polluted by the annealing with steel. The outer layer is in between the high-purity copper layer and the steel layer and is characterised by being polluted by the annealing, hence showing a low RRR [35]. The third layer is the outermost steel layer of the BS [33]. The simulations in figure 16 assumed for the inner layer a RRR $=$ 100 and a thickness of 70 μm, for the outer layer a RRR $=$ 10 and a thickness of 18 μm and a thickness of the steel layer of 1 mm. The model accurately captures the temperature dependence of the BS and its layers, with a very good agreement between the simulations and the measurements. The BS significantly affects the magnets' impedance in the frequency range between 20 Hz and about 300 Hz. Moreover, in figures 17 and 18, the simulated impedances at 35 Hz are shown by varying the RRR and thickness of the inner copper layer, as well as the RRR of the inner and outer copper

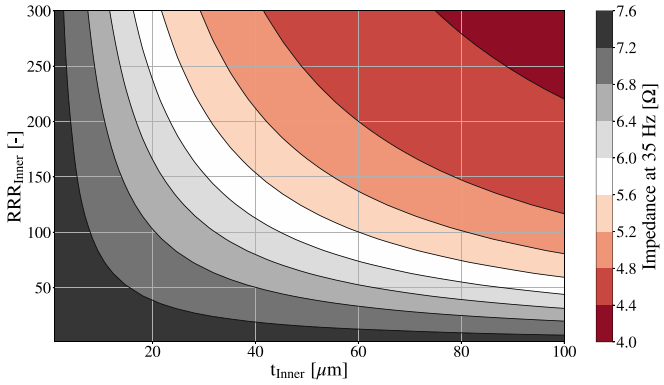

Figure 17. Simulated impedance of one LHC main dipole aperture versus thicknesses and purities of the inner copper layer of the beam screen at a frequency of 35 Hz.

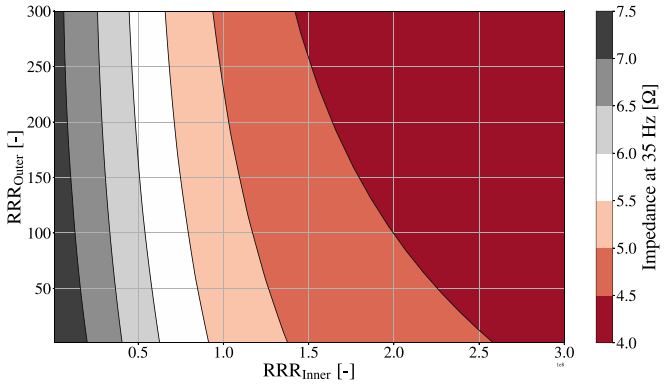

Figure 18. Simulated impedance of one LHC main dipole aperture versus purities of the beam screen's inner and outer copper layer at a frequency of 35 Hz.

layer of the BS. One can observe that the impedance is mostly affected by the purity and thickness of the inner layer while the effect of the outer layer is not negligible. Figures 17 and 18 show the simulated impedances at a small field amplitude as in TFMs. However, at larger field amplitudes, the resistivities are differently affected by the magnetoresistive effect, and hence, the impact of the outer layer becomes more significant. The choice of 35 Hz for the impedances will be motivated in the next section.

3.3. Validation of time-domain measurements

3.3.1. The LHC main dipole circuit. The LHC contains eight superconducting main dipole circuits, each comprising 154 magnets in series. The circuits are split into two branches, each containing 77 magnets. The circuit schematic is shown in figure 19. The energy extraction (EE) systems are placed between the branches, and on one side is the power converter. Each dipole has a cold diode (CD) and a resistance $R_{\mathrm{Par}} = 100\ \Omega$ in parallel. The diode is used for protection reasons to bypass the current in the case of a quench. The power converter contains an output filter with a characteristic frequency of about $f_{\mathrm{Filter}} \approx 32$ Hz [10, 43]. The differential voltage between the two apertures is used as a quench detection voltage. This differential voltage is referred to as $U_{\mathrm{QS},0} = U_1 - U_2$ [V] and triggers quench protection if it exceeds 100 mV for more than an evaluation time of 10 ms.

In the case of a FPA, the power converter is switched off, and the current bypasses the power converter through a crowbar (CB) consisting of three parallel thyristor branches. The EE resistances are switched into the current path to dissipate the energy stored in the circuit. Each of these switch openings/closings introduces voltage waves across the switches and at the output stage of the power converter filter. While the voltage wave after the disconnection of the power converter has the characteristic frequency f_{Filter} of the power converter filter, the voltage waves after switching in the EEs have a natural frequency of the circuit. The propagation time of the voltage wave through one aperture can be approximated with [10, 43]:

$$t_{\mathrm{Ap}} \approx \sqrt{L_{\mathrm{Ap}} \cdot C_{\mathrm{Gnd}}} \approx 85\ \mu\mathrm{s}, \tag{76}$$

where we assumed the nominal inductance of one aperture $L_{\mathrm{ap}} = 49$ mH and a capacitance to ground of one aperture of $C_{\mathrm{Gnd}} = 150$ nF. The natural circuit frequency is then:

$$f_{\mathrm{Circuit}} \approx \frac{1}{154 \cdot 2 \cdot t_{\mathrm{Ap}}} \approx 38\ \mathrm{Hz}. \tag{77}$$

These voltage waves then travel with the characteristic frequency along the chain of magnets, whereas each dipole introduces another phase shift to the waves.

3.3.2. Validation of time domain simulations. The equivalent network model is very computationally inexpensive and can also be used to simulate specific transients in the time domain. These transients need to show the characteristics of one specific frequency to use the magnets' respective impedance.

After the described FPA event, the voltage waves travel through the chain of magnets with the characteristic frequencies described before. An example of the voltage across one dipole magnet, compared to measurements, is shown in figure 20. One can observe the three prominent times at which the voltage wave propagates through the chain of magnets. At the moment the power converter is switched off, the voltage across each magnet drops from the ramping voltage for a ramp-rate of 10 A s^{-1} of

$$U_{\mathrm{Mag}} = \dot{I}_{\mathrm{Mag}} L \approx 0.98\ \mathrm{V}$$

to zero, while at each of the openings of the EE switches, the voltage drops correspond to

$$U_{\mathrm{Mag}} = -\frac{R_{\mathrm{EE}} \cdot I_{\mathrm{Circuit}}}{154} \quad [\mathrm{V}], \tag{78}$$

where $R_{\mathrm{EE}} = 73\ \mathrm{m}\Omega$ is the resistance of the EE and I_{Circuit} [A] the current through the circuit. For a circuit current of $I_{\mathrm{Circuit}} = 11.85$ kA, we get $U_{\mathrm{Mag}} \approx 5$ V. One can observe

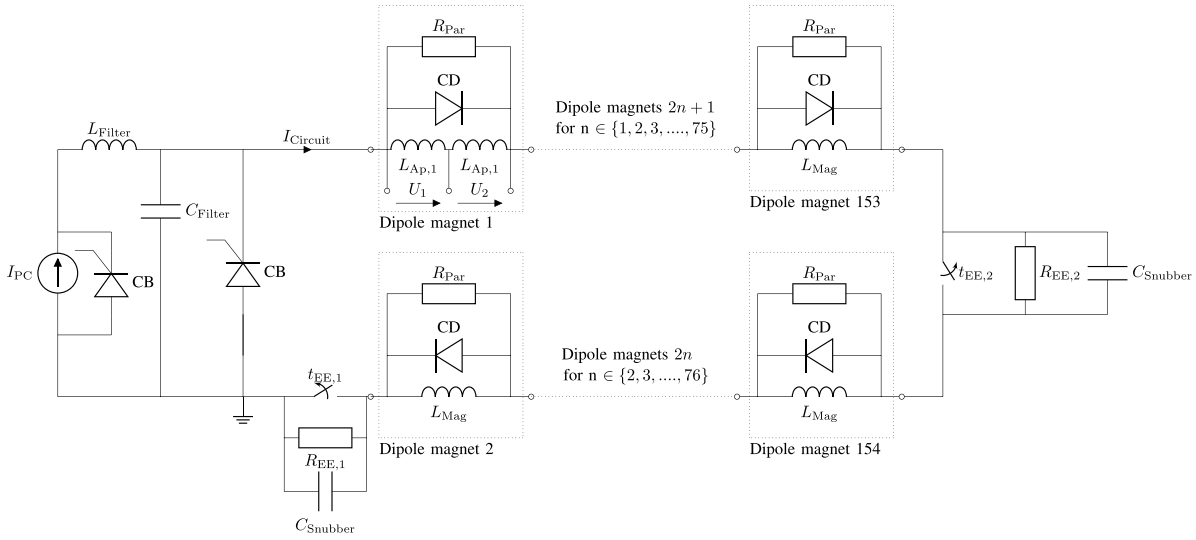

Figure 19. Simplified circuit scheme of one LHC main dipole circuit. The circuit comprises 154 magnets in series, split into two branches (odd and even branches). Each dipole has a parallel resistor R_{Par} and a cold diode (CD) in parallel. During a fast power abort (FPA), the power converter (PC) is switched off at t_{PC} and the current is then bypassed through the crowbar (CB). The two energy extraction (EE) resistances are switched into the circuit at $t_{\mathrm{EE,2}}$ and $t_{\mathrm{EE,1}}$.

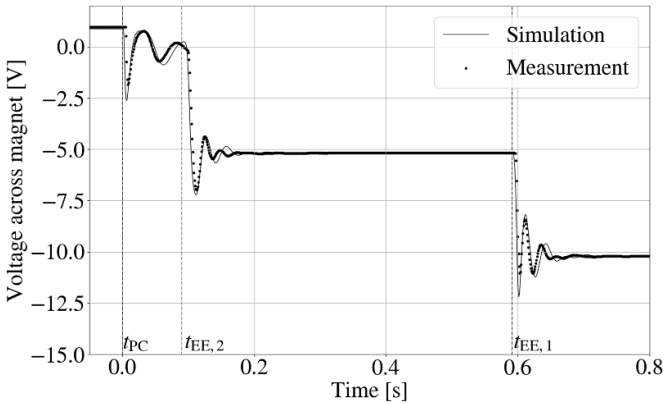

Figure 20. Measured voltage across one magnet (electrical position 25) after the switch-off of the power converter at t_{PC} and the two energy extraction switch openings $t_{\mathrm{EE,1}}$ and $t_{\mathrm{EE,2}}$ for a fast power abort at $I_{\mathrm{end}} = 11$ kA while ramping with $\mathrm{d}I/\mathrm{d}t = 10\,\mathrm{A\,s^{-1}}$.

that the voltage wave can be accurately reproduced in the simulations.

However, due to manufacturing inaccuracies, the BSs of the magnets show significant differences in their effect on the impedance. Compared to figure 17 or 18, one can observe that at the characteristic frequency of the wave, the impedance can vary significantly, up to 30%, based on the purities and thicknesses of the respective layers. If the apertures of one dipole magnet have a significantly different impedance, the voltage wave propagates at a different speed through them. As the signal $U_{\mathrm{QS,0}}$ is the difference of voltages across the apertures of each dipole, the signal picks up those differences between the apertures of the magnet at the moment the wave propagates through the magnet. This was previously modelled with equivalent parallel resistances, and good agreement was achieved [10]. However, this model did not provide any interpretability and cannot explicitly incorporate the differences in the BSs. With the equivalent network model, it becomes possible to indicate outliers whose voltage wave amplitudes can not be explained by the BS parameters.

Figure 21 compares the measurement of one $U_{\mathrm{QS,0}}$ signal and the simulation, incorporating the material differences in the BSs of the two apertures. The magnet current was ramped at $10\,\mathrm{A\,s^{-1}}$ to 2 kA during the shown event. The power converter was switched off at $t_{\mathrm{PC}} = 0$ s, while the two EEs at the end and in the middle of the chain of magnets were switched in at around $t_{\mathrm{EE,2}} = 0.1$ s and $t_{\mathrm{EE,1}} = 0.6$ s. In the case shown in figure 21, the measured $U_{\mathrm{QS,0}}$ signal reaches the threshold level of 100 mV after the disconnection of the power converter. The simulation can accurately reproduce the signal during all events: the power converter switch-off and the two switch openings.

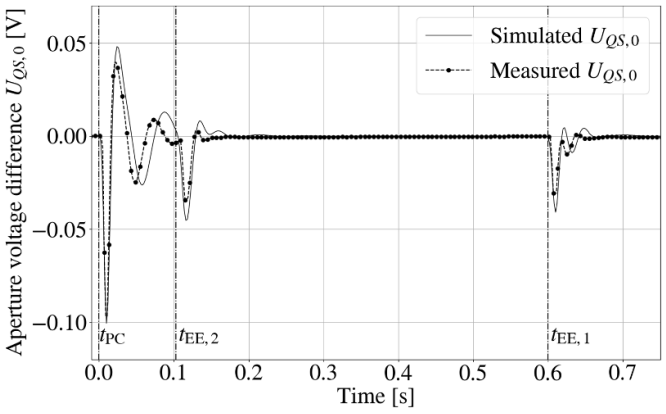

Figure 21. Measured and simulated voltage differences between the two apertures of one LHC main dipole (electrical position 25) after the switch-off of the power converter at t_{PC} and the two energy extraction switch openings $t_{EE,1}$ and $t_{EE,2}$ for a fast power abort at I_{end} =2 kA while ramping with dI/dt =10 A s^{-1}.

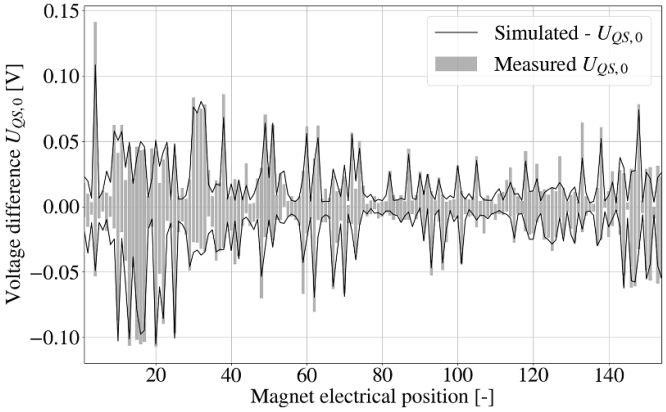

Figure 22. Comparison of simulated and measured voltage differences between the apertures in a time windowd of 0 to 50 ms after disconnecting the power converter at 2 kA with a ramp rate of 10 A s^{-1} for all 154 LHC main dipoles in one circuit.

In figure 22, the measured voltage amplitudes of the $U_{QS,0}$ signal for all 154 magnets in one circuit at the switch-off of the power converter for the same event are shown. By utilising the equivalent network model and the different BS parameters, a good accuracy of simulated and measured aperture voltage difference can be achieved for all 154 main dipoles in the chain, with an average error of about 15%. The model, hence, can be used to evaluate if the observed voltage spikes can be explained by those manufacturing inaccuracies or if different reasons must be considered.

4. Discussion

The impedance analysis provides some valuable insights into the electrodynamic behaviour of a superconducting magnet, which is useful for future prototypes of accelerator magnets to minimise energy losses and optimise operational efficiency. Eddy currents or other non-linear coupling effects within a magnet could cause unexpected voltage behaviour or losses. The presented fast transients in the main dipole circuits serve as an example, during which spurious triggering of the quench detection systems due to impedance differences between the magnets' apertures present a problem.

When considering coupling effects within an accelerator magnet, there are generally two governing parameters that mostly affect the impedance of a magnet. The first one is the time constant of the eddy currents. The larger the time constant, the smaller the frequencies at which those eddy currents occur. Generally, the time constant is inversely proportional to the material's resistivity in which the currents are induced. Naturally, superconductors with infinite conductivity hence cause PCs to flow at low frequencies. Similarly, coupling currents, such as IFCC or ISCC, flow through the superconductor and only shortly cross through low-resistivity material. Considerations to avoid or reduce the resulting losses are already well-known in the literature. However, other materials often used in accelerator magnets, such as copper, aluminium, or bronze alloys, also have significant conductivity and could hence cause significant losses in certain frequency regimes. Moreover, defining tighter as well as upper- and lower-bounded manufacturing requirements for these components could avoid different impedances between apertures or a series of magnets. These differences could cause unexpected voltage behaviour and, for example, cause spurious triggering of protection systems. Special attention should be paid to whether magnet components should be made with these materials.

The second governing parameter is the loop size that the induced currents will form. The larger these loops, the larger the equivalent inductance and coupling of the effect with the magnet would be and, hence, the more significant the impact on the magnets' impedance. The loop size scales with the longitudinal length of the component to consider, as well as with its volume and especially its thickness in the cross-section. However, in some cases, the currents also close through other components or materials and, hence, combine multiple volumes with each other. For example, one can consider the effect of the presented coil protection sheets in the case of the LHC main dipole. Even though these sheets are thinner than 1 mm, they impact the magnets' impedance significantly. The sheets are over the full length of the magnet and placed on both sides of an aperture. As these sheets are not insulated from each other, the currents are induced longitudinally along the sheets and then close through the metallic collars, creating a significantly bigger loop. Such eddy currents can be avoided or reduced by either considering a sufficient lamination of the component or insulation between the respective volumes.

5. Conclusion and outlook

This contribution proposes an equivalent lumped-element model incorporating various coupled, non-linear, interdependent physical coupling and magnetisation effects. These effects are included in the network model as loops, consisting of an inductance and resistance, that can be calculated by analytical

equations or derived from finite-element simulations. The derivation of the included effects was described. Even though the presented model is applied to a specific type of accelerator magnet and comes with assumptions, the general modelling principle can be applied to other types of magnets straightforwardly.

The model was validated on a wide range of available measurement data in the frequency- and time-domain. First, the simulation results were compared to the measured complex impedance of a stand-alone LHC main dipole in the CERN magnet test facility. The simulation and the measurement show a very good agreement with a general error of around 5%. Moreover, a very good agreement was achieved for comparing the complex impedance of the LHC main dipole and the simulations at various temperatures between cryogenic and room temperature.

The model was further validated with measurements from the main dipoles, that are installed in the LHC. The model can accurately reproduce the effects of different materials and purities used in the CPSs and BSs on the magnet's differential inductance and their interdependence with the conductor coupling effects. The general error is below 5%.

As such, the equivalent network model is very computationally inexpensive and, hence, can simulate the electromagnetic behaviour of a full LHC main dipole circuit consisting of 154 main dipoles in series. FPA events were simulated using the equivalent network model, including specific material parameters for the different LHC main dipoles. These cause impedance differences between the magnets and as well between their apertures, causing voltage differences. These voltage differences are successfully reproduced by the model and are in agreement with the measurements.

It was shown that the equivalent network model can accurately reproduce a wide range of scenarios in the time- and frequency-domain. Moreover, the model preserves a very high level of interpretability, as it incorporates individual parameters and features of specific effects, such as different materials or purities, and it can provide valuable insight into each effect's impact on the overall electromagnetic behaviour. As such, the model can be used to investigate further if observed outliers in measurements can be correctly classified as outliers or if these could be caused by manufacturing tolerances. Moreover, the network model can also be used to explore the effects of failures, such as inter-turn shorts, on the electromagnetic behaviour.

Data availability statement

All data that support the findings of this study are included within the article (and any supplementary files).

Acknowledgment

The authors would like to thank the CERN ELQA team, in particular, G D'Angelo and J Ludwin; the CERN SM18 team, in particular, R Bouvier and G Ninet, as well as the CERN HWC teams, in particular, M Solfaroli, for their help in the measurements. This work was supported by the Wolfgang Gentner Programme of the German Federal Ministry of Education and Research (Grant No. 13E18CHA).

Appendix A. Derivation of equivalent lumped-element parameter for PCs in superconductors

To calculate the equivalent parameter for the proposed equivalent coupling loop, one has to compare the power definitions of the electrical equivalent network and physically derived formulas for the PCs.

The transferred power $P_{\mathrm{PC,Ph}}$ due to the PCs consists of the stored and lost power and can be described as, starting from equations (53) and (51):

$$\begin{aligned}
P_{\mathrm{PC,Ph}} &= P_{\mathrm{Stored}} + P_{\mathrm{Loss}} \qquad (79)\\
&= \int_V \left(\mathbf{H}\frac{\mathrm{d}\mathbf{B}}{\mathrm{d}t}\right)\mathrm{d}V + \int_V \left(\mathbf{M}\frac{\mathrm{d}\mathbf{B}}{\mathrm{d}t}\right)\mathrm{d}V\\
&= \int_V (\mathbf{H}+\mathbf{M})\frac{\mathrm{d}\mathbf{B}}{\mathrm{d}t}\mathrm{d}V\\
&= \int_V \left(\frac{f_{\mathrm{H}}}{\mu_0}I_{\mathrm{Mag}} + \frac{I_{\mathrm{PC}}}{d_{\mathrm{s}}}\right)\cdot\frac{\mathrm{d}}{\mathrm{d}t}\left(\mu_0(\mathbf{H}+\mathbf{M})\right)\mathrm{d}V\\
&= \int_V \left(\frac{f_{\mathrm{H}}}{\mu_0}I_{\mathrm{Mag}} + \frac{I_{\mathrm{PC}}}{d_{\mathrm{s}}}\right)\cdot\frac{\mathrm{d}}{\mathrm{d}t}\left(\mu_0\frac{f_{\mathrm{H}}}{\mu_0}I_{\mathrm{Mag}} + \mu_0\frac{I_{\mathrm{PC}}}{d_{\mathrm{s}}}\right)\mathrm{d}V\\
&= \int_V \left(\frac{f_{\mathrm{H}}}{d_{\mathrm{s}}}I_{\mathrm{Mag}}\frac{\mathrm{d}I_{\mathrm{PC}}}{\mathrm{d}t}\right) + \left(\frac{1}{\mu_0}f^2{}_{\mathrm{H}}I_{\mathrm{Mag}}\frac{\mathrm{d}I_{\mathrm{Mag}}}{\mathrm{d}t}\right)\\
&\quad + \left(\frac{f_{\mathrm{H}}}{d_{\mathrm{s}}}I_{\mathrm{PC}}\frac{\mathrm{d}I_{\mathrm{Mag}}}{\mathrm{d}t}\right) + \left(\mu_0\frac{1}{d_{\mathrm{s}}^2}I_{\mathrm{PC}}\frac{\mathrm{d}I_{\mathrm{PC}}}{\mathrm{d}t}\right)\mathrm{d}V\\
&= \underbrace{\left(V_{\mathrm{s}}\frac{f_{\mathrm{H}}}{d_{\mathrm{s}}}I_{\mathrm{Mag}}\frac{\mathrm{d}I_{\mathrm{PC}}}{\mathrm{d}t}\right)}_{=\text{ Term 1}} + \underbrace{\left(L_{\mathrm{Mag}}I_{\mathrm{Mag}}\frac{\mathrm{d}I_{\mathrm{Mag}}}{\mathrm{d}t}\right)}_{=\text{ Term 2}}\\
&\quad + \underbrace{\left(V_{\mathrm{s}}\frac{f_{\mathrm{H}}}{d_{\mathrm{s}}}I_{\mathrm{PC}}\frac{\mathrm{d}I_{\mathrm{Mag}}}{\mathrm{d}t}\right)}_{=\text{ Term 3}} + \underbrace{\left(V_{\mathrm{s}}\frac{\mu_0}{d_{\mathrm{s}}^2}I_{\mathrm{PC}}\frac{\mathrm{d}I_{\mathrm{PC}}}{\mathrm{d}t}\right)}_{=\text{ Term 4}}, \qquad (80)
\end{aligned}$$

with V_{S} [m^3] the strand volume and where we used the following assumptions and relations:

$$\mathbf{B} = \mu_0(\mathbf{M}+\mathbf{H}) \qquad [\mathrm{T}], \qquad (81)$$

$$\mathbf{H} = \frac{f_{\mathrm{H}}}{\mu_0}I_{\mathrm{Mag}} \qquad \left[\mathrm{A\,m^{-1}}\right], \qquad (82)$$

$$L_{\mathrm{Mag}} = \int_V \frac{1}{\mu_0}f^2{}_{\mathrm{H}}\mathrm{d}V \qquad [\mathrm{H}], \qquad (83)$$

$$\mathbf{M} = \frac{I_{\mathrm{PC}}}{d_{\mathrm{s}}} \qquad \left[\mathrm{A\,m^{-1}}\right]. \qquad (84)$$

The third relation describes the relation between the magnetic transfer function and the magnet's self-inductance. Moreover, it can be shown that a $\cos(\theta)$ current distribution on the outside of a round conductor generates a uniform magnetisation and that the total induced current needed to generate this magnetisation follows equation (84) [21, 30].

The total power in the equivalent loop of the network model, as presented in figure 3, $P_{\mathrm{PC,El}}$ can be described by:

$$\begin{aligned} P_{\mathrm{PC,El}} &= I_{\mathrm{Mag}} V_{\mathrm{Mag}} + I_{\mathrm{PC}} V_{\mathrm{PC}} \\ &= I_{\mathrm{Mag}} \left(L_{\mathrm{Mag}} \frac{\mathrm{d}I_{\mathrm{Mag}}}{\mathrm{d}t} + M_{\mathrm{ec,PC}} \frac{\mathrm{d}I_{\mathrm{PC}}}{\mathrm{d}t} \right) \\ &\quad + I_{\mathrm{PC}} \left(L_{\mathrm{PC}} \frac{\mathrm{d}I_{\mathrm{PC}}}{\mathrm{d}t} + M_{\mathrm{ec,PC}} \frac{\mathrm{d}I_{\mathrm{Mag}}}{\mathrm{d}t} \right) \\ &= \underbrace{M_{\mathrm{ec,PC}} I_{\mathrm{Mag}} \frac{\mathrm{d}I_{\mathrm{PC}}}{\mathrm{d}t}}_{=\text{ Term 1}} + \underbrace{L_{\mathrm{Mag}} I_{\mathrm{Mag}} \frac{\mathrm{d}I_{\mathrm{Mag}}}{\mathrm{d}t}}_{=\text{ Term 2}} \\ &\quad + \underbrace{M_{\mathrm{ec,PC}} I_{\mathrm{PC}} \frac{\mathrm{d}I_{\mathrm{Mag}}}{\mathrm{d}t}}_{=\text{ Term 3}} + \underbrace{L_{\mathrm{PC}} I_{\mathrm{PC}} \frac{\mathrm{d}I_{\mathrm{PC}}}{\mathrm{d}t}}_{=\text{ Term 4}} . \end{aligned} \tag{85}$$

By comparing the highlighted terms in equations (80) and (85), one can immediately find the definition for the inductance and mutual coupling of the equivalent loop for a single strand:

$$L_{\mathrm{ec,PC}} = \frac{V_{\mathrm{s}}}{d_{\mathrm{s}}^2} \mu_0 = \mu_0 \frac{\pi}{4} l_{\mathrm{mag}} \qquad [\mathrm{H}],$$

$$M_{\mathrm{ec,PC,1}} = \frac{V_{\mathrm{s}}}{d_{\mathrm{s}}} f_{\mathrm{H}} = \frac{\pi}{4} d_{\mathrm{s}} l_{\mathrm{mag}} f_{\mathrm{H}} \qquad [\mathrm{H}].$$

Appendix B. Derivation of the field attenuation factor α

One starts by considering a conductive, non-magnetic domain Γ with a constant permeability under the impact of an externally applied, harmonic magnetic vector potential $\mathbf{A}_{\boldsymbol{a}}$ [Tm] of the form:

$$\mathbf{A}_{\boldsymbol{a}} = \mathbf{A}_z \sin(\omega t). \tag{86}$$

This applied magnetic vector potential generates eddy currents $\mathbf{J}_{\boldsymbol{i}}$ [A m^2] in the conductive domain, which in turn generates an additional magnetic vector potential $\mathbf{A}_{\boldsymbol{i}}$. We will use the definition:

$$\mathbf{B} = \nabla \times \mathbf{A}, \tag{87}$$

$$\nabla \cdot \mathbf{A} = 0. \tag{88}$$

We start by considering the parabolic magnetic diffusion equation for the magneto-quasistatic case in a dimensionless form [23]:

$$\nabla^2 \mathbf{B} = \tau \frac{\mathrm{d}}{\mathrm{d}t} \mathbf{B}, \tag{89}$$

with $\tau = \frac{\mu l_0^2}{\rho}$ [s] the magnetic diffusion time constant and l_0 [m] the conductor dimension. The magnetic flux density consists of the applied $\mathbf{B}_{\boldsymbol{a}}$ and induced field $\mathbf{B}_{\boldsymbol{i}}$:

$$\mathbf{B} = \mathbf{B}_{\boldsymbol{i}} + \mathbf{B}_{\boldsymbol{a}}. \tag{90}$$

We notice the relation:

$$\nabla^2 \mathbf{B} = \underbrace{(\nabla \cdot \nabla)\mathbf{B}}_{=0} - \nabla \times \nabla \times \mathbf{B}$$

where the first term on the right-hand side equals zero as defined by the Gauss–Faraday law. Moreover, as the applied field is generated externally, beyond the region of interest, we assume it has zero curl:

$$\nabla \times \mathbf{B}_a = 0$$

Inserting equation (90) into (89), and using the relations above we obtain:

$$\nabla^2 (\mathbf{B}_{\boldsymbol{a}} + \mathbf{B}_{\boldsymbol{i}}) = \tau \frac{\mathrm{d}}{\mathrm{d}t} \mathbf{B} \tag{91}$$

$$\nabla \times \nabla \times (\mathbf{B}_{\boldsymbol{a}} + \mathbf{B}_{\boldsymbol{i}}) = -\tau \frac{\mathrm{d}}{\mathrm{d}t} \mathbf{B} \tag{92}$$

$$\underbrace{\nabla \times \nabla \times \mathbf{B}_{\boldsymbol{a}}}_{=0} + \nabla \times \nabla \times \mathbf{B}_{\boldsymbol{i}} = -\tau \frac{\mathrm{d}}{\mathrm{d}t} \mathbf{B} \tag{93}$$

$$\nabla \times \mathbf{A}_{\boldsymbol{i}} = -\tau \frac{\mathrm{d}}{\mathrm{d}t} \nabla \times \mathbf{A} \tag{94}$$

$$\nabla \times \mathbf{A}_{\boldsymbol{i}} = -\tau \nabla \times \frac{\mathrm{d}}{\mathrm{d}t} \mathbf{A} \tag{95}$$

$$\mathbf{A}_{\boldsymbol{i}} = -\tau \frac{\mathrm{d}}{\mathrm{d}t} \mathbf{A}. \tag{96}$$

We notice the form of a first-order linear time-invariant system for the magnetic vector potential.

Now, we assume a solution for the induced field inside the conducting domain of the form [11]:

$$\mathbf{A}_{\boldsymbol{i}} = -\mathbf{A}_z \cos(\omega t - t_n) \sin(t_n), \tag{97}$$

with the substitution:

$$t_n = \tan^{-1}(\omega \tau). \tag{98}$$

The new vector potential, including the induced term, then results in the following:

$$\mathbf{A}_{\mathbf{Tot}} = \mathbf{A}_{\boldsymbol{a}} + \mathbf{A}_{\boldsymbol{i}} \tag{99}$$

$$= \mathbf{A}_z \sin(\omega t) - \mathbf{A}_z \cos(\omega t - t_n) \sin(t_n) \tag{100}$$

$$= \mathbf{A}_z \sin(\omega t - t_n) \cos(t_n). \tag{101}$$

One can observe that the exciting magnetic field potential inside this conductive domain is being retarded by a time $\frac{t_n}{\omega}$ and the magnitude is being attenuated by a factor $\cos(t_n)$, which are both an increasing function of τ. We can rewrite this attenuation and introduce the new field attenuation factor:

$$\gamma = \cos(t_n) = \frac{1}{\sqrt{1 + (\omega\tau)^2}} \qquad [-]. \tag{102}$$

One can observe the following limits for γ:

$$\lim_{\omega \to 0} \gamma = 1 \tag{103}$$

$$\lim_{\omega \to \infty} \gamma = 0. \tag{104}$$

Equation (101) then can be rewritten into the expanded trigonometric form of:

$$\mathbf{A}_{\mathbf{Tot}} = \mathbf{A}_z \gamma (\omega\tau \cos(\omega t) + \gamma \sin(\omega t)). \tag{105}$$

One can now identify the shape of a complex number with the real and imaginary part:

$$\Re\left(\mathbf{A_{Tot}}\right) = \mathbf{A}_z \gamma \omega \tau, \tag{106}$$

$$\Im\left(\mathbf{A_{Tot}}\right) = \mathbf{A}_z \gamma^2, \tag{107}$$

where we can conclude with the field attenuation factor:

$$\alpha = \left(\gamma\omega\tau + j \cdot \gamma^2\right). \tag{108}$$

ORCID iDs

M Janitschke https://orcid.org/0000-0002-8931-7199
E Ravaioli https://orcid.org/0000-0002-7651-5313
U van Rienen https://orcid.org/0000-0003-1042-2058

References

[1] Ehmler H, Fillunger H, Baldzuhn J, Maix R, Jeckle A, Parodi S, Rummel T, Ribe K and Scheller H 2006 Comparative analysis of impulse and impedance tests to detect short circuits within the W7-X magnets *IEEE Trans. Appl. Supercond.* **16** 767–70

[2] Rißе K, Rummel T, Ehrke G and Koppen M 2010 Design, tests and repair procedures for the electrical insulation of the superconducting W7-X magnets *IEEE Trans. Appl. Supercond.* **20** 447–50

[3] Ehmler H, Dixon I R, Painter T A and Powell J A 2012 Electrical AC tests on CICC coil for series-connected hybrid magnet *IEEE Trans. Appl. Supercond.* **22** 9002204

[4] Foussat A, Grand-Clement L, Smekens D, Pincot F O, Bortot L and Savary F 2018 Frequency-domain diagnosis methods for quality assessment of Nb_3Sn coil insulation systems and impedance measurement *IEEE Trans. Appl. Supercond.* **28** 1–5

[5] Obermair C, Apollonio A, Charifoulline Z, Felsberger L, Janitschke M, Pernkopf F, Ravaioli E, Verweij A, Wollmann D and Wozniak M 2024 Interpretable anomaly detection in the LHC main dipole circuits with non-negative matrix factorization *IEEE Trans. Appl. Supercond.* **34** 1–12

[6] Shafer R E 1980 Eddy currents, dispersion relations, and transient effects in superconducting magnets *Technical Report* FERMILAB-TM-991 (FERMILAB, Batavia, IL)

[7] Smedley K M and Shafer R E 1994 Experimental determination of electrical characteristics and circuit models of superconducting dipole magnets *IEEE Trans. Magn.* **30** 2708–12

[8] Dahlerup-Petersen K and Schmidt F 1995 Impedance measurements and modeling of the ten metre prototype LHC dipole magnet *Technical Report* (LHC-Project-Note-11 CERN, Geneva)

[9] Bourgeois F and Dahlerup-Petersen K 2001 Methods and results of modeling and transmission-line calculations of the superconducting dipole chains of CERN's LHC collider *LHC-Project-Report-497*

[10] Ravaioli E, Dahlerup-Petersen K, Formenti F, Steckert J, Thiesen H and Verweij A 2012 Modeling of the voltage waves in the LHC main dipole circuits *IEEE Trans. Appl. Supercond.* **22** 9002704

[11] Shafer R 1980 Eddy currents, dispersion relations, and transient effects in superconducting magnets (available at: https://ieeexplore.ieee.org/stamp/stamp.jsp?arnumber=1061171)

[12] Ambjorndalen S 2017 Determination of AC characteristics of superconducting dipole magnets in the large hadron collider based on experimental results and simulations (available at: https://cds.cern.ch/record/2280571)

[13] Liakopoulou A, Annema A J, Bortot L, Charifoulline Z, Maciejewski M, Prioli M, Ravaioli E, Salm C, Schmitz J and Verweij A P 2020 Analysis of short-circuit transients in the LHC main dipole circuit *J. Phys.: Conf. Ser.* **1559** 012077

[14] Martino M 2022 Low-frequency analytical model of superconducting magnet impedance *Model. Simul. Eng.* **2022** 1–13

[15] Wolstrup A F, Ravaioli E, Zsurzsan T G and Zhang Z 2021 Automatic frequency-domain modelling of superconducting magnets and its usability to model general inductors *2021 IEEE 12th Energy Conversion Congress & Exposition - Asia (ECCE-Asia)* pp 1312–8

[16] Szwangruber P B *et al* 2024 Electrical simulations of the SIS100 superconducting dipole and quadrupole circuits: Transients, earthing and failure modes *IEEE Trans. Appl. Supercond.* **34** 1–5

[17] Janitschke M, Bednarek M, Ravaioli E, Verweij A, Willering G, Wozniak M and van Rienen U 2024 Validating the physics-driven lumped-element model of the LHC main dipole magnet *IEEE Trans. Appl. Supercond.* **34** 1–5

[18] Verweij A P 1995 Electrodynamics of superconducting cables in accelerator magnets *PhD Dissertation* Twente U., Twente

[19] Wilson M 1983 *Superconducting Magnets* (*Monographs on Cryogenics*) (Clarendon)

[20] Bortot L, Auchmann B, Cortes Garcia I, Fernandez Navarro A M, Maciejewski M, Prioli M and Schöps S 2017 A 2-D finite-element model for electrothermal transients in accelerator magnets *IEEE Trans. Magn.* **54** 7000404

[21] Ravaioli E, Auchmann B, Maciejewski M, ten Kate H and Verweij A 2016 Lumped-element dynamic electro-thermal model of a superconducting magnet *Cryogenics* **80** 346–56

[22] Russenschuck S 2010 *Field Computation for Accelerator Magnets: Analytical and Numerical Methods for Electromagnetic Design and Optimization* (Wiley)

[23] Knoepfel H E 2000 *Magnetic Field Diffusion and Eddy Currents* (Wiley) Ch. 4, pp 153–234

[24] Turck B Losses in superconducting multifilament composites under alternating changing fields (available at: www.osti.gov/biblio/6165478)

[25] Turck B 1979 Coupling losses in various outer normal layers surrounding the filament bundle of a superconducting composite *J. Appl. Phys.* **50** 5397–401

[26] Morgan G H 1970 Theoretical behavior of twisted multicore superconducting wire in a time-varying uniform magnetic field *J. Appl. Phys.* **41** 3673–9

[27] Carr W J 1974 AC loss in a twisted filamentary superconducting wire *J. Appl. Phys.* **45** 929–38

[28] Sorbi M and Marinozzi V 2016 Magnetization heat in superconductors and in eddy current problems: a classical thermodynamic approach *IEEE Trans. Appl. Supercond.* **26** 1–9

[29] Campbell P 2000 Comments on energy stored in permanent magnets *IEEE Trans. Magn.* **36** 401–3

[30] Ravaioli E 2020 Persistent-currents magnetization in STEAM-LEDET *Technical Report* EDMS 2418186 (CERN Geneva)

[31] Bean C P 1962 Magnetization of hard superconductors *Phys. Rev. Lett.* **8** 250–3

[32] Bean C P 1964 Magnetization of high-field superconductors *Rev. Mod. Phys.* **36** 31–39

[33] Cruikshank P *et al* 1998 Mechanical design aspects of the LHC beam screen (available at: https://cds.cern.ch/record/330853)
[34] Namjoshi K and Biringer P 1988 Low-frequency eddy-current loss estimation in long conductors by using the moment of inertia of cross sections *IEEE Trans. Magn.* **24** 2181–5
[35] Kos N 2002 GDOES analyses of 50 and 75 microns OFE copper layer beam screen samples, produced by HEREAUS *Technical Report* EDMS 340852 v.1 (CERN, Geneva)
[36] Brüning O, Collier P, Lebrun P, Myers S, Ostojic R, Poole J and Proudlock P 2004 *LHC Design Report* Geneva: CERN
[37] Sandia National Laboratories 2023 Xyce parallel electronic simulator Version 7.8 (available at: https://xyce.sandia.gov/)
[38] Rossi L 2003 The LHC main dipoles and quadrupoles toward series production *IEEE Trans. Appl. Supercond.* **13** 1221–8
[39] Ravaioli E *et al* 2016 First implementation of the CLIQ quench protection system on a 14-m-long full-scale LHC dipole magnet *IEEE Trans. Appl. Supercond.* **26** 1–5
[40] Charifoulline Z 2006 Residual resistivity ratio (RRR) measurements of LHC superconducting NbTi cable strands *IEEE Trans. Appl. Supercond.* **16** 1188–91
[41] Jiles D 1992 A self consistent generalized model for the calculation of minor loop excursions in the theory of hysteresis *IEEE Trans. Magn.* **28** 2602–4
[42] Bergqvist A 1996 A simple vector generalization of the Jiles-Atherton model of hysteresis *IEEE Trans. Magn.* **32** 4213–5
[43] Ravaioli E *et al* 2012 Impact of the voltage transients after a fast power abort on the quench detection system in the LHC main dipole chain *IEEE Trans. Appl. Supercond.* **22** 9002504